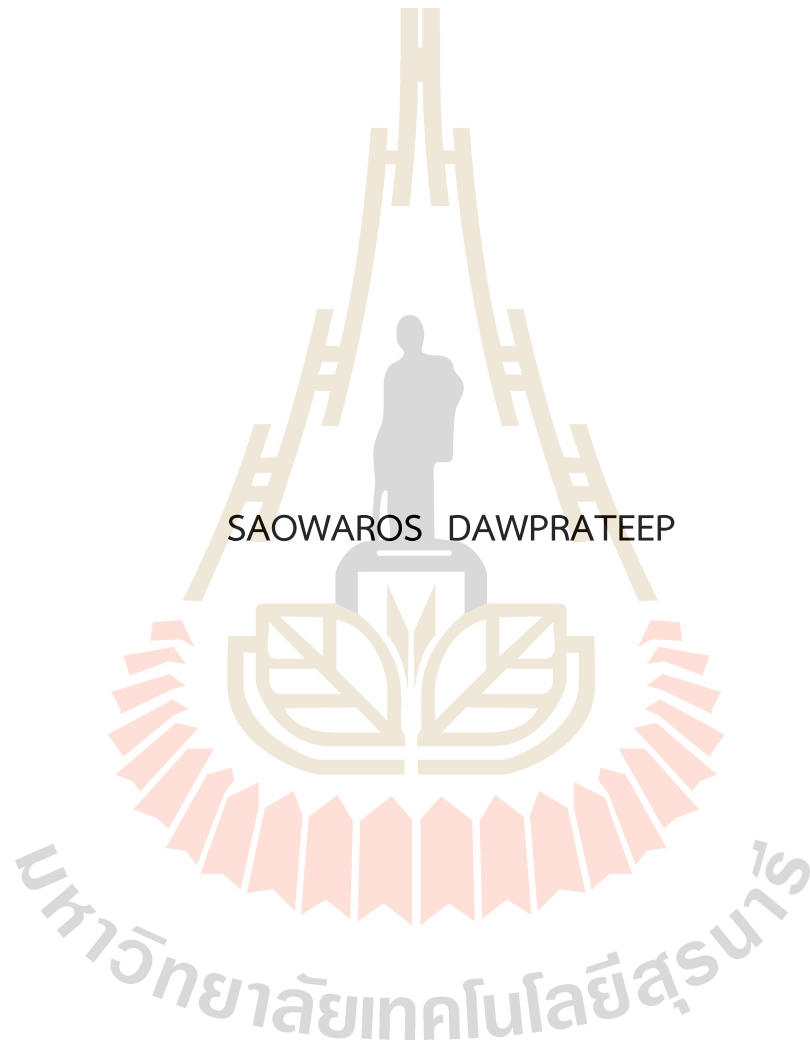


PARTICLE SIZE EXTRACTION FROM IN-LINE HOLOGRAMS
BY USING THE MINIMUM OF THE SINGLE COEFFICIENT
OF THE WIGNER-VILLE DISTRIBUTION



A Thesis Submitted in Partial Fulfillment of the Requirements for the
Degree of Doctor of Philosophy in Applied Physics
Suranaree University of Technology
Academic Year 2022

การสกัดขนาดอนุภาคจากอินไลน์ไฮโดแกรมโดยใช้ค่าสัมประสิทธิ์ต่ำสุด
หนึ่งเดียวของการกระจายวิกเนอร์-วิลต์



นางสาวเสาวรส ดาวประทีป

วิทยานิพนธ์นี้เป็นส่วนหนึ่งของการศึกษาตามหลักสูตรปริญญาวิทยาศาสตรดุษฎีบัณฑิต

สาขาวิชาฟิสิกส์

มหาวิทยาลัยเทคโนโลยีสุรนารี

ปีการศึกษา 2565

PARTICLE SIZE EXTRACTION FROM IN-LINE HOLOGRAMS BY USING
THE MINIMUM OF THE SINGLE COEFFICIENT
OF THE WIGNER-VILLE DISTRIBUTION

Suranaree University of Technology has approved this thesis submitted in partial fulfillment of the requirements for the Degree of Doctor of Philosophy.

Thesis Examining Committee



(Assoc. Prof. Dr. Panomsak Meemon)

Chairperson



(Prof. Dr. Joewono Widjaja)

Member (Thesis Advisor)



(Assoc. Prof. Dr. Eckart Schulz)

Member



(Asst. Prof. Dr. Boonsong Sutapun)

Member



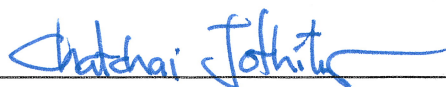
(Dr. Siriwat Soontaranon)

Member



(Prof. Dr. Santi Maensiri)

Dean of Institute of Science



(Assoc. Prof. Dr. Chatchai Jothityakoon)

Vice Rector for Academic Affairs

and Quality Assurance

เสาวรส ดาวประทีป : การสกัดขนาดอนุภาคจากอินไลน์โฮโลแกรมโดยใช้ค่าสัมประสิทธิ์ต่ำสุดหนึ่งเดียวของการกระจายวิกเนอร์-วิลล์ (PARTICLE SIZE EXTRACTION FROM IN-LINE HOLOGRAMS BY USING THE MINIMUM OF THE SINGLE COEFFICIENT OF THE WIGNER-VILLE DISTRIBUTION) อาจารย์ที่ปรึกษา : ศาสตราจารย์ ดร.ยูวโน วิตจายา, 84 หน้า.

คำสำคัญ: การถ่ายภาพโฮโลแกรมแบบดิจิทัล, การกระจายวิกเนอร์-วิลล์, การวัดขนาดอนุภาคแบบเส้น, การสร้างรูปร่างของอนุภาคแบบ 3 มิติ,

วิทยานิพนธ์นี้จัดทำขึ้นเพื่อเสนอวิธีการใหม่ในการสกัดขนาดอนุภาคจากอินไลน์โฮโลแกรมโดยใช้ค่าสัมประสิทธิ์หนึ่งเดียวของการกระจายวิกเนอร์-วิลล์ (ดับเบิลยูวีดี) มีข้อดีคือสามารถทำการวัดขนาดของอนุภาคได้โดยไม่ต้องคำนึงถึงการหาตำแหน่งของอนุภาค ซึ่งส่งผลให้วิธีการที่นำเสนอมีความรวดเร็วและแม่นยำกว่าวิธีการอื่น ๆ ที่จำเป็นต้องทราบตำแหน่งของอนุภาคก่อนเสมอ วิธีการที่เสนอนี้สามารถพัฒนาเพิ่มเติมได้คือการนำไปประยุกต์ใช้กับการสร้างโปรไฟล์ของอนุภาคทรงเส้นในรูปแบบ 3 มิติ โดยการเพิ่มข้อมูลเกี่ยวกับตำแหน่งของอนุภาคที่ได้รับจากการกระจายวิกเนอร์-วิลล์ความเป็นไปได้ของวิธีการวัดขนาด และการสร้างรูปของวัตถุที่นำเสนอสามารถพิสูจน์ได้จากการยืนยันเชิงการทดลองโดยการวิเคราะห์ข้อมูลได้จากอินไลน์โฮโลแกรมของหลอดไมโครพลาสติกชนิดโพลีคาร์บอเนตที่มีขนาดเส้นผ่าศูนย์กลาง 80 และ 100 ไมโครเมตร โฮโลแกรมของอนุภาคที่มีการวางมุม และตำแหน่งต่าง ๆ กันถูกบันทึกโดยใช้เซ็นเซอร์ซีซีดี และเลเซอร์ความยาวคลื่น 543.5 นาโนเมตร การวิเคราะห์เชิงทฤษฎีเกี่ยวกับประสิทธิภาพของวิธีการที่นำเสนอนี้ แสดงให้เห็นว่าช่วงของการวัดขนาดของอนุภาค และการสร้างใหม่นั้นขึ้นอยู่กับระยะเวลาการบันทึก และความละเอียดของเซ็นเซอร์

สาขาวิชาฟิสิกส์
ปีการศึกษา 2565

ลายมือชื่อนักศึกษา เสาวรส ดาวประทีป
ลายมือชื่ออาจารย์ที่ปรึกษา ดร.ยูวโน วิตจายา

SAOWAROS DAWPRATEEP : PARTICLE SIZE EXTRACTION FROM IN-LINE HOLOGRAMS BY USING THE MINIMUM OF THE SINGLE COEFFICIENT OF THE WIGNER-VILLE DISTRIBUTION. THESIS ADVISOR : PROF. JOEWONO WIDJAJA, Ph.D.
84 PP.

Keyword: Digital holography, Wigner-Ville distribution, Line-shaped particle sizing, 3D particle reconstruction

This thesis presents a new method for extracting the size of line-shaped particles from in-line holograms using a single coefficient of the Wigner-Ville distribution (WVD). The advantages of this proposed method are that the size of the particle can be measured without searching for particle position as in the conventional methods. Besides having a faster response, it is free from errors in depth-search. The proposed method has been further developed for 3D profile reconstruction of the line-shaped particles using the information on particle depth position obtained using the WVD. The sizing and reconstruction feasibilities of the proposed method are experimentally verified by analyzing in-line holograms of 80 and 100 μm diameter polycarbonate microtubes. The holograms were recorded at different orientations and depth positions with a 543.5 nm laser and CCD sensor. Theoretical analysis of the performance of the proposed method shows that the ranges of size measurement and reconstruction are dependent on the recording distance and the sensor resolution.

School of Physics
Academic Year 2022

Student's Signature Saowaros Dawprateep
Advisor's Signature Joewono Widjaja

ACKNOWLEDGEMENTS

I would like to thank the following people who have helped me complete my thesis with their advice and assistance.

My deepest gratitude goes firstly and foremost to my thesis advisor, Prof. Dr. Joewono Widjaja, for giving me a chance, motivation, and advice throughout my Ph.D. study.

I would like to thank Assoc. Prof. Dr. Panomsak Meemon, Assoc. Prof. Dr. Eckart Schulz, Asst. Prof. Dr. Boonsong Sutapun, and Dr. Siriwat Soontaranon for offering me a variety of great suggestions.

I would like to thank Suranaree University of Technology for the financial support provided through the scholarship.

I also would like to thank all the lecturers in the School of Physics at the Suranaree University of Technology who have taught and developed my knowledge in the past academic years.

I would like to thank all of the teachers and lecturers I have had in my life who taught me everything I know.

Finally, I'd like to thank my parents for their support in completing my studies.

Saowaros Dawprateep

CONTENTS

	Page
ABSTRACT IN THAI.....	I
ABSTRACT IN ENGLISH.....	II
ACKNOWLEDGEMENTS.....	III
CONTENTS.....	IV
LIST OF TABLES.....	VI
LIST OF FIGURES.....	VIII
LIST OF ABBREVIATIONS.....	XII
CHAPTER	
I INTRODUCTION.....	13
1.1 Background.....	13
1.2 Significance of the study.....	17
1.3 Research objectives.....	18
1.4 Scope and limitation of the study.....	18
1.5 Organization.....	18
II HOLOGRAPHY.....	19
2.1 Hologram recording.....	19
2.1.1 Digital In-line Holography (DIH).....	20
2.2 Numerical reconstruction.....	24
2.2.1 Angular spectrum method (ASM).....	24
2.3 Particle Analysis.....	26
2.3.1 Particle position.....	26
2.3.2 Particle size.....	28
2.3.3 Particle orientation and length.....	29
III WIGNER-VILLE DISTRIBUTION.....	31
3.1 Wigner-Ville distribution (WVD).....	31
3.2 WVD of in-line hologram.....	32

CONTENTS (Continued)

	Page
3.2.1 The WVD coefficient with minimum amplitude	36
3.2.2 Previous WVD-based particle sizing	39
3.3 Proposed extraction of particle size using a single WVD coefficient with minimum amplitude	41
3.4 Particle sizing performance	42
3.5 Particle tracking using a single WVD coefficient with minimum amplitude	44
3.6 3D reconstruction of line-shaped particles.....	45
IV EXPERIMENTAL VERIFICATIONS.....	52
4.1 Experimental setup.....	52
4.2 Experimental verifications of particle sizing from holograms.....	55
4.2.1 Experimental verifications of the particle sizing using the flip and replication technique (FRT).....	61
4.2.2 Experimental verifications of the size measurement from the in-line hologram of rotated particles	62
4.2.3 Reconstructions of 3D profile of the rotated particle.....	72
V CONCLUSIONS AND THE FUTURE WORK	76
5.1 Conclusions	76
5.2 Future work	77
REFERENCES	78
CURRICULUM VITAE.....	84

LIST OF TABLES

Table		Page
3.1	The range of the index of l of cosine terms in Eq. (3.6).	35
3.2	Range of the measurable size, position and length of the line-shaped particle from the digital holograms using the proposed WVD.	50
4.1	Range of measurable particle sizes using the proposed method for recording distances of 10 - 15 cm.	55
4.2	Mean of the detected spatial frequencies of the minimum WVD coefficient and the mean absolute errors (MAEs) in the size measurement of microtube with the diameter $2a = 80 \mu\text{m}$ and the rotation angles $\alpha = 90^\circ$, $\beta = 0^\circ$ and $\gamma = 90^\circ$ in the x-y plane by using the proposed single WVD coefficient.	59
4.3	Mean of the detected spatial frequencies of the minimum WVD coefficient and the mean absolute errors (MAEs) in the size measurement the microtube with the diameter $2a = 100 \mu\text{m}$ and the rotation angles $\alpha = 90^\circ$, $\beta = 0^\circ$ and $\gamma = 90^\circ$ in the x-y plane by using the proposed single WVD coefficient.	60
4.4	Mean of the detected spatial frequencies of the minimum WVD coefficient and the mean absolute errors (MAEs) in the size measurement of the microtube with the diameter $2a = 80 \mu\text{m}$ and $100 \mu\text{m}$ and the rotation angles $\alpha = 90^\circ$, $\beta = 0^\circ$ and $\gamma = 90^\circ$ by using the FRT one time.	61
4.5	Errors in measurement of the depth z and the size a from the recorded holograms of the microtube parallel to the yz plane at the angles $\alpha = 90^\circ$, $\beta = 60^\circ$ and $\gamma = 30^\circ$	65
4.6	MAEs in the position and size measurements of the $100 \mu\text{m}$ microtube oriented parallel to the xz plane at the angles $\alpha = 50^\circ$, $\beta = 40^\circ$ and $\gamma = 90^\circ$ using the proposed single WVD coefficient.	68

LIST OF TABLES (Continued)

Table	Page
4.7 MAEs in the position and size measurements of the 100 μm microtube oriented diagonally in the 3D space, $\alpha = 45^\circ$, $\beta = 60^\circ$ and $\gamma = 60^\circ$ using the proposed single WVD coefficient.	72
4.8 The orientation angles and length of the 100 μm microtube oriented parallel to the yz plane for difference recording distances.....	72
4.9 The orientation angles and length of the 100 μm microtube oriented diagonally in the 3D space for difference recording distances.	74



LIST OF FIGURES

Figure	Page
2.1 A schematic diagram for recording (a) the digital in-line hologram and (b) the digital off-axis holography (DOH).....	20
2.2 (a) 2-D simulated in-line hologram of the line-shaped particle with the size $a = 50 \mu\text{m}$ recorded with $\lambda = 543.5 \text{ nm}$ at the distance $z = 15 \text{ cm}$ and (b) its corresponding intensity transmittance.	22
2.3 1D simulated in-line hologram of the line-shaped particle with the size $a = 40 \mu\text{m}$ and $50 \mu\text{m}$ recorded at the distance $z = 15 \text{ cm}$	23
2.4 The intensity impulse response of the wave propagation through free space.	25
2.5 The corresponding transfer function of Figure 2.4.	25
2.6 Comparisons between the 1D cross-sectional scan of image intensities reconstructed from the hologram of the $100 \mu\text{m}$ line-shaped particle recorded at the wrong and the correct distance $z = 30 \text{ cm}$	26
2.7 Particle size measurement at the FWHM by using the Fresnel diffraction integral and the angular spectrum method.....	28
2.8 Flowchart for particle analysis.	29
3.1 (a) The simulated 1-D in-line hologram signal shown in Figure 2.2(b) with a background removal for the positive x axis and (b) the corresponding WVD of the in-line hologram of Figure 3.1(a).	33
3.2 Distribution of the WVD coefficients obtained by using Eq. (3.6) with $N = 5$, $2a = 100.00 \mu\text{m}$, $z = 15 \text{ cm}$, and $\lambda = 543.5 \text{ nm}$	36
3.3 Comparison of 1-D plots along the slope of the WVD coefficients of Eqs. (3.8) with WVD of the original hologram in Figure 3.1(b).	37
3.4 1-D plots along the corresponding slope of the 31 st , 32 nd and 33 rd components of WVD.....	38

LIST OF FIGURES (Continued)

Figure	Page
3.5 Plots of the WVD coefficients scanned along the slopes $1/\lambda z$ for the particle sizes $a = 40$ and $50 \mu\text{m}$, respectively.	38
3.6 The WVD coefficients of the in-line hologram for $z = 15 \text{ cm}$ scanned at $x = L/2$	40
3.7 Flowchart for the particle size extraction using the peak position of W_{Ia1} and W_{Ia63} along the frequency axis at $x = L/2$	40
3.8 Flowchart of the line-shaped particle sizing using the single spatial frequency information of the WVD coefficient with minimum amplitude.....	42
3.9 A flow chart for extracting the particle position from the in-line hologram with the WVD coefficient with minimum amplitude.	44
3.10 Recording geometry of hologram of a line-shaped particle in 3-D space.	46
3.11 The recorded hologram of the line-shaped particle with an arbitrary orientation in 3-D space.....	47
3.12 1-D cross-sectional scan of the hologram fringe for measuring the angle α	47
3.13 Plot of the resultant averaged position of the fringe center as a function of the row.....	48
3.14 The vertically oriented hologram after the rotation with the angle $90^\circ - \alpha$	49
3.15 A flow chat for plotting 3D profile of particles using the proposed method.	51
4.1 A schematic diagram of an optical setup for recording the digital in-line holograms of the microtube with different orientation in 3-D space.....	52
4.2 A microtube mounted on a rotating mount.....	53
4.3 A combination of two rotating mounts to rotate the microtube in 3-D space.	53
4.4 Experimental setup for the verifications of the proposed method.	54

LIST OF FIGURES (Continued)

Figure	Page
4.5 (a) The in-line hologram of the 100 μm microtube recorded at the distance $z = 15$ cm with the rotation angles $\alpha = 90^\circ$, $\beta = 0^\circ$ and $\gamma = 90^\circ$ and (b) its background intensity.....	56
4.6 Normalized 1D intensity of the recorded particle hologram shown in Figure 4.5(a) and its corresponding simulation with the background removal.....	57
4.7 The WVD outputs of the holograms recorded at the axial distance $z = 15$ cm. The particle diameters are (a) 80 and (b) 100 μm , respectively.....	58
4.8 Plots of the WVD coefficients scanned along the slopes $1/\lambda z$ of Figure 4.7(a) and (b).....	59
4.9 The hologram of the 100 μm microtube oriented parallel to the yz plane with the angle $\alpha = 90^\circ$, $\beta = 60^\circ$ and $\gamma = 30^\circ$, and the recording distance $z = 14$ cm.....	62
4.10 1D cross-sectional intensities of the hologram in Figure 4.9, which were scanned along (a) the 20 th and (b) the 440 th rows, respectively.....	63
4.11 Plots of the measured depth position z for different recording distances of the holograms of the microtube parallel to the yz plane as a function of the row numbers represented in mm unit.....	64
4.12 (a) The hologram of the microtube oriented parallel to the xy plane with the angle $\alpha = 50^\circ$, $\beta = 40^\circ$ and $\gamma = 90^\circ$ at the recording distance $z = 14$ cm. (b) The vertically oriented hologram after the rotation with the angle $90^\circ - \alpha$	66
4.13 1D cross-sectional intensities of the hologram shown in Figure 4.12(b), which were scanned along (a) the 250 th and (b) the 450 th rows, respectively.....	67

LIST OF FIGURES (Continued)

Figure	Page
4.14 (a) The hologram of the 100 μm microtube diagonally oriented in 3D space with the angles $\alpha = 45^\circ$, $\beta = 60^\circ$, and $\gamma = 60^\circ$, and the recording distance $z = 14$ cm. (b) The vertically oriented hologram after the rotation with the angle $90^\circ - \alpha$	69
4.15 1D cross-sectional intensities of the hologram in Figure 4.14(b), which scanned along (a) the 250 th and (b) the 450 th rows, respectively.....	70
4.16 Plots of the measured depth position z for different recording distances of the holograms as a function of the row numbers represented in mm unit.....	71
4.17 3D reconstructed profile of the 100 μm microtube profile oriented parallel in the yz plane using the proposed method. The hologram was recorded at the recording distance z of 14 cm.	73
4.18 3D profile of the reconstructed particle of $z = 14$ cm from the recorded in-line hologram of a line-shaped particle with $a = 50$ μm and the rotation angle $\alpha = 45$, $\beta = 60$, and $\gamma = 60$ degrees.....	75

LIST OF ABBREVIATIONS

2D	Two Dimensional
3D	Three Dimensional
ASM	Angular Spectrum Method
CCD	Charge-Coupled Device
DIH	Digital In-line Holography
DOH	Digital Off-axis Holography
FRT	Flip and Replication Technique
FWHM	Full Width at the Half Maximum
LAP	Laplacian Operator
LDV	Laser Doppler Velocimetry
MAE	Mean Absolute Error
PDA	Phase Doppler Anemometry
PIV	Particle Image Velocimetry
VAR	Variance Operator or Variance of Gray Value Distribution
WVD	Wigner- Ville Distribution

CHAPTER I

INTRODUCTION

1.1 Background

Particle size and shape can have a significant impact on the production and efficacy of special chemicals used in medicines, food, dyes, textiles, and cosmetics (Khanam et al., 2011). Smaller particles generally have a larger surface area to volume ratio, which can increase reactivity and solubility. This can lead to faster and more efficient chemical reactions, making the production process more efficient. Additionally, smaller particles can also improve the dispersion and absorption of the chemical, leading to better efficacy. On the other hand, larger particles can be easier to handle and may have better mechanical properties, such as increased strength and stability. The shape of the particle can also impact its behavior; for example, a spherical particle will have a different flow behavior than a needle-shaped particle. Overall, the particle size and shape can play a crucial role in the properties and effectiveness of the final chemical product. The study of extracting information from particles by using light tends to increase in many fields of study (Hariharan, 2007). The reason for this interest is that using light allows for the non-destructive analysis of particles and for multiple measurements to be taken on the same sample. The particles can be analyzed without causing any damage and it is easy for scientists to develop their skills through trial and error. This is known as non-intrusive laser optical measurement (Misono, 2019). One of the optical techniques that uses light to extracting information from small particles is laser Doppler velocimetry (LDV). LDV measures the velocities of flowing particles by using the Doppler effect, where a monochromatic laser beam with a known frequency is split into two crossing beams in order to produce an interference area. When the particle passes through the interference area, light scattered by the particle is detected by a photomultiplier. The scattered light frequency is changed

according to the Doppler shift effect. The particle velocity can be calculated as a multiplication of the fringe spacing by the change in frequency (Yeh and Cummins, 1964). The LDV technique is fast and highly accurate for measuring the velocity of small particles, and it can also be applied to different particles, such as flow of red blood cells (Kilpatrick, Tyberg and Parmley, 1982; Memmolo et al., 2014), micro-fiber (Bou et al., 2019), and sizing of spray-droplets (Bachalo, 1980).

Phase Doppler anemometry (PDA) is an optical technique based on the LDV technique that can measure not only the velocity but also the size of the particles. This technique uses two photodetectors with different fields of view to extract different phases of the detected interference signals. The phase difference between the two detected signals is directly proportional to the size of the particle. This technique has a fast-sizing response. However, it can not measure large particles because the phase difference may become greater than 2π (Xie, Dou and Zhou, 2016). The limitations of both techniques, LDV and PDA, are:

- The observation area is limited as the LDV is a single-point measurement.
- They can measure only particles with a low aspect ratio such as spherical particles.
- There is no shape information.

The number of measurement points can be increased by using particle image velocimetry (PIV) (Willert and Gharib, 1991). In the PIV technique, the flowing particles are recorded in a two-dimensional (2-D) plane (Wereley and Meinhart, 2010) or 3-D space (Zhang et al., 2014) by a combination of a pulse laser and a single or two cameras. To track the movement of particles, a correlation between the first recorded image and the next recording is calculated. The PIV has higher accuracy in tracking and sizing particles (Kohli, 2012). However, its setup is more complicated than the LDV technique.

On the other hand, the 3-D shape of particles can be reconstructed by using holography, which is also a non-intrusive optical technique. In-line holography,

invented by Gabor in 1948, is an interference technique for recording the amplitude and phase of light waves diffracted by small objects (Gabor, 1948). The recording process requires a monochromatic light wave to illuminate the objects being studied. An interference of two waves that are diffracted by the objects and the un-diffracted light is recorded onto either a photosensitive medium or an array image sensor. Since it is based on diffraction phenomena, the recorded light pattern, called a hologram, contains 3-D information of the object. In accordance with the recording medium, the in-line holography provides either an analog or digital hologram (Buters and Lendertz, 1971; Schnars and Jüptner, 1994). The advantage of holography is that the 3-D particle information is recorded without changing the physical configurations and characteristics of the particles. There is barely any other invention that has had more influence on the optical sciences than holograms. (Caulfield, 2004; Gabor, 1984).

Consequently, the extractions of particle information can be done by means of the diffraction process. In digital in-line holography (DIH), the extraction is performed by solving numerically the angular spectrum method or the Fresnel diffraction integral of the digital hologram (Kim, 2010). Owing to the unknown axial position of the particle, the numerical extraction is done for different reconstruction distances. In order to obtain the correct axial position of the particle, the contrast of the edges of the reconstructed image is then measured using a variance operator (VAR) or Laplacian operator (LAP). The reconstructed image with the highest contrast gives the correct axial position (Kim and Lee, 2007; Memmolo et al., 2015). Both techniques are good at measuring the contrast of the reconstructed image from the holograms with low particle density, where the particle separation is large (Seo and Lee, 2014). There exist also other techniques such as weighted spectral analysis and an absolute gradient calculation (GAR) (Langehanenberg et al., 2008).

The numerical reconstruction method combined with the contrast measurement has also been applied in different fields of science and technology. In biomedical science, a short-coherence light source has been used to record digital holograms from backscattered light from dense tissue. Since, a hologram can preserve the phase information of a light wave, phase modulation caused by intracellular

motions in living tissue can be recorded. Therefore, the recorded hologram can be used to study the shape and motility of tumor spheroids (Merrill, An, Turek and Nolte, 2015), while the study of motility, shape, and viability of live sperm cells using the DIH was reported by Caprio et al. (Caprio et al., 2014). The DIH was also used in ophthalmic instruments to provide a set of high-contrast images of engraved marks in progressive addition lenses. This is because conventional visual inspection is difficult to identify and characterize engraving marks that are often faint, weak, obscured by scratches and partially occluded on tinted or antireflection-coated lenses (Perucho and Micó, 2014). Shao, Li and Hong (Shao, Li and Hong, 2019), proposed a new technique for the measuring the instantaneous gas leakage rate from a ventilated supercavity generated in a water tunnel using the DIH. Besides being low cost, compact, and high-resolution, the technique can be used for characterizing low void fraction bubbly flow in a broad range of applications. Recently, tomographic imaging of blood coagulation structures using digital holographic microscopy was reported by Funamizu and Aizu (Funamizu and Aizu, 2018). By recording digital holograms of rotating red blood cells, complete 3-D structures and refractive index distributions can be successfully reproduced. This method has advantages over different tomographic methods using quantitative phase imaging in that the proposed system is low-cost, portable, and able to provide complete 3-D structures of red blood cells, which have high aspect ratios. Furthermore, besides the above advantages, the DIH has also been found to be a very safe method for studying interactions between rod-shaped *Escherichia coli* bacteria and their physical environments (McCartney et al., 2001; Molaei and Sheng, 2014; Bianchi, Saglimbeni and Leonardo, 2017) and the identification of bacterial species (Buzalewicz et al., 2016).

The conventional holographic particle sizing requires many steps of calculation, such as the numerical reconstruction followed by the contrast measurement and the sizing step itself. Therefore, the computational cost is high. To solve this problem, different algorithms for extracting the particle size and its axial position from holograms without numerical reconstruction have been proposed using a wavelet transform (Soontaranon, Widjaja and Asakura, 2008). This is because the wavelet transform is a multi-resolution signal representation that can be used to analyze non-stationary

holographic signals. However, its limitation is that the wavelet transformation requires many window functions.

Instead of the wavelet transform, the holographic particle tracking and sizing can also be done by using the Wigner-Ville distribution (WVD). The WVD is a joint space-frequency signal representation. Unlike the wavelet transform, the WVD employs a single window function. Therefore, the WVD computation is simpler and more straightforward. In the WVD analysis of the particle hologram, the particle axial position can be tracked by determining either the slope of the WVD coefficients with the maximum peak (Chuamchaitrakool, Widjaja and Yoshimura, 2015) or the single WVD coefficient with the minimum peak (Widjaja, Dawprateep and Chuamchaitrakool, 2017). In the case of WVD-based particle sizing, the size is calculated by using local spatial-frequency information at the half length of the holograms being analyzed, provided that the particle position is known.

1.2 Significance of the study

Our previous study found an important finding: the particle size can be calculated from the WVD coefficients along the spatial frequency axis at the half length of the hologram. Therefore, WVD analysis of the particle holograms is very useful for extracting 3-D information without the use of conventional numerical reconstructions and the focus function, which are iterative and time-consuming.

In real-world problems such as the mentioned studies of red blood cells and microorganisms, the required object position is generally unknown. In order to solve this limitation, the present research work proposes a new method for particle sizing from in-line holograms without the need to first track their positions. This proposed method is implemented by further taking advantage of the single WVD coefficient (Widjaja, Dawprateep and Chuamchaitrakool, 2017). Consequently, the proposed method has advantages over our previous works in that, firstly, errors in measuring the particle size are not affected by the accuracy of the particle tracking. Secondly, the

calculation technique is simpler without sacrificing accuracy. Finally, its measurement response is shorter, because tracking the particle position is unnecessary.

1.3 Research objectives

- To propose a method for sizing a line-shaped particle from the in-line digital holograms by using a single WVD coefficient without the need to know its position information.
- To reconstruct the 3D profile of the line-shape particle from the in-line digital holograms by using the proposed WVD method.
- To verify the feasibility of the proposed method through experiments.

1.4 Scope and limitation of the study

- Test particles are opaque microtubes with diameters of 80.0 and 100.0 micrometers.
- The feasibility of the proposed method is experimentally verified.

1.5 Organization

This thesis consists of five chapters. This first chapter gives an introduction to the thesis. In Chapter II, the fundamentals of digital holography, numerical techniques for image reconstructions, and particle information extraction are reviewed. In Chapter III, the theory of the WVD and the WVD coefficient with minimum amplitude are presented. Its applications to the sizing and 3D reconstruction of the line-shaped particle are discussed. Chapter IV presents the experimental verifications of the proposed method. The conclusions of the thesis are provided in Chapter V.

CHAPTER II

HOLOGRAPHY

Following the invention of coherent laser light, the interference of two light waves, an object wave and a reference wave, results in the coding of an object's information (Goodman and Lawrence, 1967). The recording and the reconstruction of the object image are referred to as holograms, while the technique for producing a three-dimensional image of the object is called as holography. The main difference between holography and photography is that in holography, the phase of the object wave that depends on the object depth can be preserved. The second difference is that holography can be done without a focusing lens. In this chapter, the fundamentals of holography are introduced. Numerical reconstruction from digital particle holograms by using the angular spectrum method is discussed with a focus on the extraction of the particle size and orientation.

2.1 Hologram recording

Dennis Gabor got the Nobel Prize in 1971 for his original invention of in-line holography in 1948 (Gabor, 1948). He was trying to make an electron microscope for atomic-level analysis. The result was a new holographic work that would affect the science of electron holography and optical holography 10-20 years later. At the time holography was introduced, the recording of the hologram was done using a photographic film. Since the development of digital sensor in holography, digital holography has been widely used in many fields of science and technology (Meyer-Arendt, 1989). In the study of small particles, the digital hologram encodes information about the particle such as position, size, and orientation. 3-D particle information recorded in the digital holograms can be extracted via a numerical reconstruction method. Digital hologram recording is separated into two main types depending on

the path of the light in the recording setups, such as digital in-line holography and digital off-axis holography. The details of both are as follows.

2.1.1 Digital In-line Holography (DIH)

Figure 2.1(a) shows a schematic diagram of an optical setup for recording the particle hologram by using Gabor's in-line setup with a laser light source operating at a wavelength of λ .

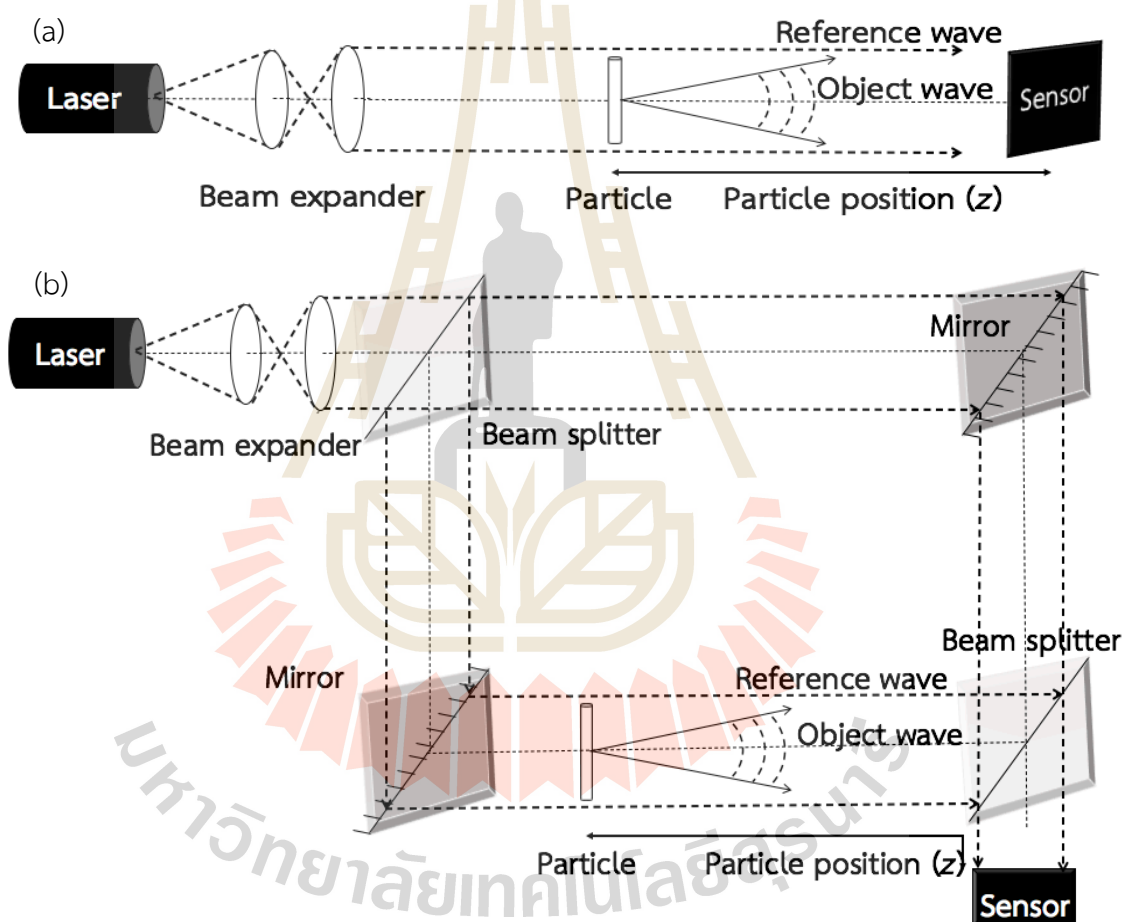


Figure 2.1 A schematic diagram for recording (a) the digital in-line hologram and (b) the digital off-axis holography (DOH).

The schematic diagrams of the optical setup for recording the hologram are shown in Figure 2.1(a): in-line holography and (b) off-axis holography. Both setups are non-intrusive to the particle environment or the particles themselves. Figure 2.1(a) shows the simple design of the hologram recording of a digital in-line hologram. In

contrast, in DOH in Figure 2.1(b), the collimated light has been separated into two beams with a constant distance (Wopschall and Pampalone, 1972), which makes device alignment more complex and complicated. When comparing both techniques, the reconstructed image does not show much difference (Latychevskaia et al., 2010). However, the DIH setup is simple and requires less equipment, making DIH cheaper and more attractive. An example of one use for in-line holography is to extract the information of the particles from the interference fringe of the in-line hologram from a single-shot picture (Li et al., 2020).

Consider a rod-shaped particle with a diameter of $2a$. that is illuminated by a collimated beam. The beam collimation provides a wide analyzable region of the particle distribution. The diffracted object wave and the reference wave are recorded by the charge-coupled device (CCD) sensor at position z . After recording the interference pattern by the sensor, the intensity transmittance of the hologram can be expressed as (Tyler and Thompson, 1976)

$$I(x) = \left\{ 1 - \frac{4a}{\sqrt{\lambda z}} \cos\left(\frac{\pi x^2}{\lambda z} - \frac{\pi}{4}\right) \left(\frac{\sin\left(\frac{2\pi ax}{\lambda z}\right)}{\frac{2\pi ax}{\lambda z}}\right) + \frac{4a^2}{\lambda z} \left(\frac{\sin\left(\frac{2\pi ax}{\lambda z}\right)}{\frac{2\pi ax}{\lambda z}}\right)^2 \right\} \text{rect}\left(\frac{x}{2L}\right), \quad (2.1)$$

where $2L$ is the width of the CCD sensor. Hence, the recorded hologram is limited by the sensor's length of $2L$. The background intensity of light is represented by the first term. The second term is the product of a cosine chirp function with a sinc function. The cosine chirp function has a space-varying frequency, which is inversely proportional to the product of the wavelength λ and the recording distance z . The sinc function represents the diffraction of the particle. The width of the sinc's main lobe is proportional to the ratio of the wavelength to the particle size, λ/a . A comparison of the amplitudes of the third term and the previous terms reveals that the square of the sinc function is significantly lower, allowing the third term to be ignored (Murata, Fujiwara and Asakura, 1970).

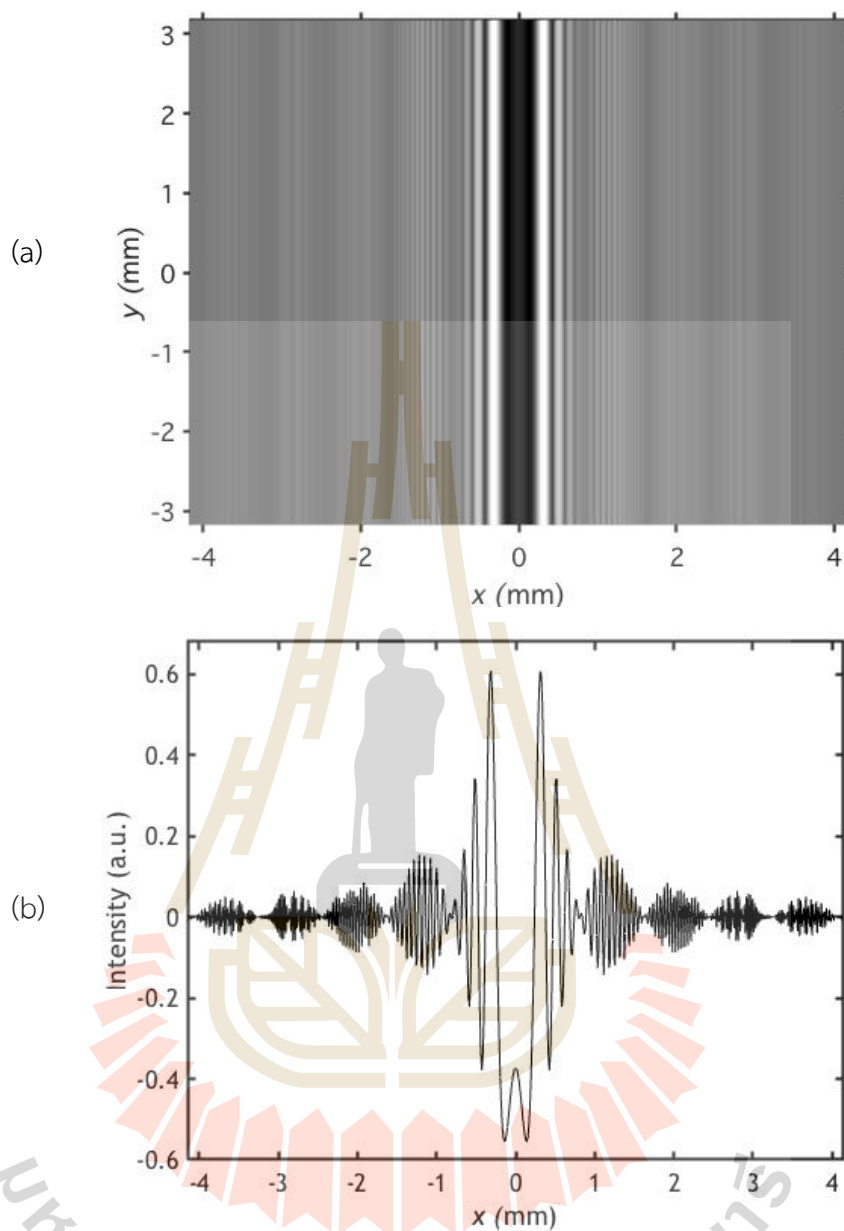


Figure 2.2 (a) 2-D simulated in-line hologram of the line-shaped particle with the size $a = 50 \mu\text{m}$ recorded with $\lambda = 543.5 \text{ nm}$ at the distance $z = 15 \text{ cm}$ and (b) its corresponding intensity transmittance.

An in-line hologram of the line-shaped particle that is oriented in the vertical direction is shown in Figure 2.2(a). The hologram is simulated with a particle size $2a$ of $100 \mu\text{m}$ at a distance z of 15 cm and a wavelength of 543.5 nm . The sensor has an area of $6.4 \text{ mm} \times 8.3 \text{ mm}$. Figure 2.2(b) is the corresponding plot of the 1-D intensity transmittance along the horizontal direction. The space-varying fringe frequency

caused by the second term of Eq. (2.1) can be clearly observed in figure 2.2(b). For a shorter recording distance, the frequency of the cosine fringe increases rapidly. Since the spatial resolution of the digital image sensor is limited, the hologram is potentially under-sampled. This is the limitation of digital in-line holography. To avoid this limitation, the hologram recording must satisfy the Nyquist sampling theorem (Laughton and Warne, 2003) that is the highest chirp frequency must be smaller or equal to two times of a sampling frequency of the sensor.

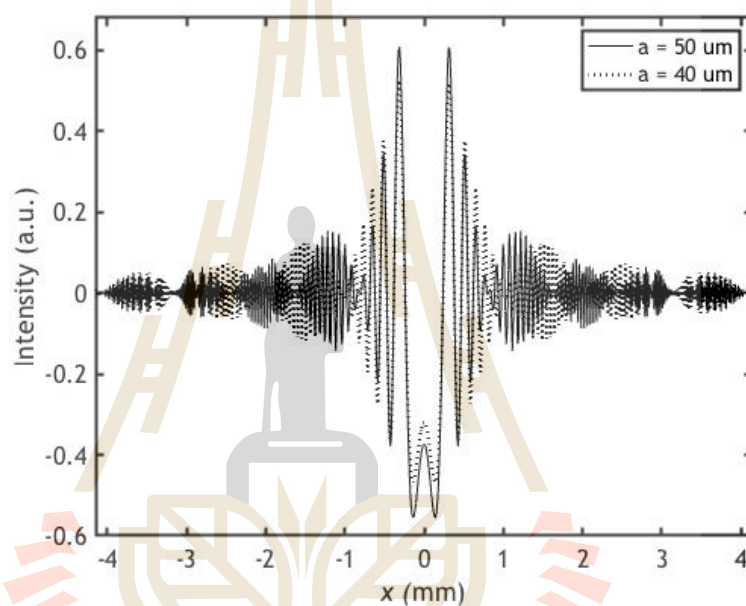


Figure 2.3 1D simulated in-line hologram of the line-shaped particle with the size $a = 40 \mu\text{m}$ and $50 \mu\text{m}$ recorded at the distance $z = 15 \text{ cm}$.

Figure 2.3 shows the simulated intensity transmittance of the holograms of line-shaped particles with a diameter of 80 and 100 μm at the distance $z = 15 \text{ cm}$. They are simulated using the second and third terms of Eq. (2.1). It is obvious that the hologram contains the particle size, as the envelope of the hologram fringe is broad when the size of the particle is small. The digital in-line holography is efficient for measuring the size of the small particles. And it is a non-intrusive technique to the particle environment, or even the particles themselves. To extract the information of the particles from the interference fringe of the in-line hologram, the reconstruction process is always used to measure particle size and orientation. The reconstruction process is reviewed in the next section.

2.2 Numerical reconstruction

In DIH, each image particle needs to be reconstructed at a different distance along the optical axis. This is because of the unknown particle position. This is similar to searching for the best-focused image reconstruction in optical holography. The best-focused image is reconstructed at the correct distance. To find the correct particle position, the sharpness of each reconstructed image is measured using a focus function. The particle size is determined by measuring the full width at the half maximum of the reconstructed image.

2.2.1 Angular spectrum method (ASM)

Due to its fast computational algorithm, the angular spectrum method has been widely applied in particle analysis to obtain the position, size, and orientation of the particle from the digital holograms (Yu and Kim, 2005). The angular spectrum method is a mathematical representation for calculating the propagation of optical fields in homogeneous media. The reconstruction using the angular spectrum method is mathematically defined as

$$U(x, y) = \mathcal{F}^{-1}\{\mathcal{F}(U(\xi, \eta)) \times H(f_x, f_y)\}. \quad (2.2)$$

where \mathcal{F} and \mathcal{F}^{-1} denote the Fourier transform and its inverse transform, respectively. $U(\xi, \eta)$ and $U(x, y)$ represent the wave fields of the hologram and the reconstructed image, respectively. According to the Eq. (2.2), the reconstruction process can be done by taking the inverse Fourier transform of the multiplication of the hologram's spectrum and the transfer function $H(f_x, f_y)$ of the propagation through free space given by (Goodman, 1996)

$$H(f_x, f_y) = \begin{cases} \exp\left[(ikz)\sqrt{1 - (\lambda f_x)^2 - (\lambda f_y)^2}\right], & \sqrt{f_x^2 + f_y^2} < \frac{1}{\lambda} \\ 0 & \text{otherwise.} \end{cases} \quad (2.3)$$

The transfer function is derived by considering the propagation of the angular spectrum as a linear spatial filter. Equation (2.3) shows that wave components are rapidly attenuated outside a circular boundary of radius $1/\lambda$ in the frequency plane.

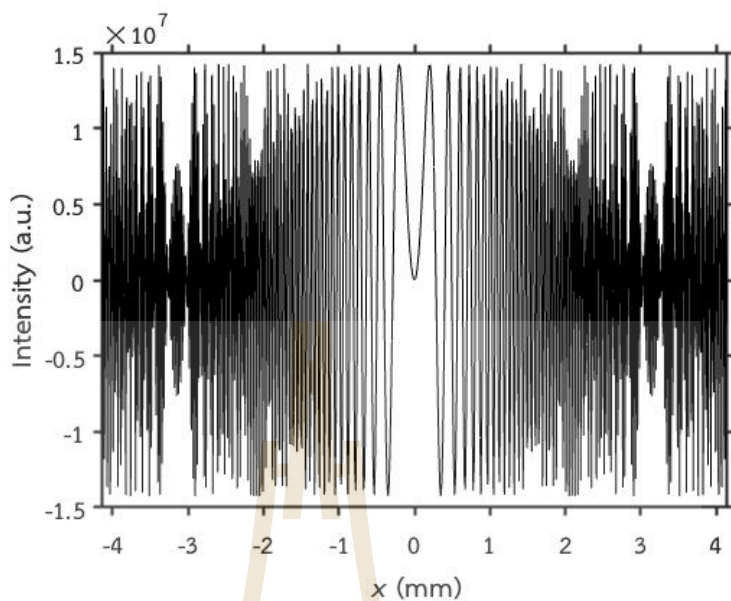


Figure 2.4 The intensity impulse response of the wave propagation through free space.

Plots of the intensity of the impulse response and the transfer function of the wave propagation through free space are shown in Figures 2.4 and 2.5, respectively. They are generated by calculating Eq. (2.4) with a wavelength of 543.5 nm at a distance of $z = 10$ cm using the Matlab program. The plots demonstrate the holograms' nonstationary nature.

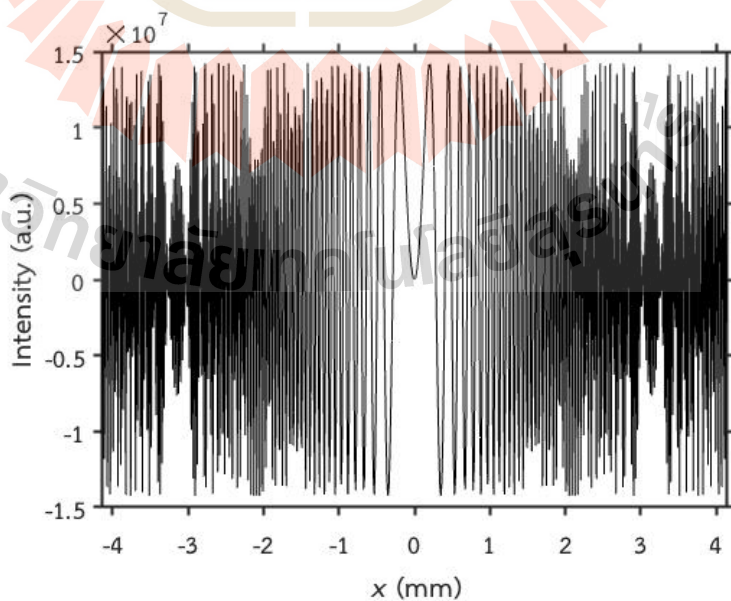


Figure 2.5 The corresponding transfer function of Figure 2.4.

Figure 2.6 shows comparisons between the reconstructed image of the 100 μm particle holograms recorded at the distance of $z = 30$ cm. The numerical reconstructions at the wrong positions of 20 and 40 cm broaden the resultant images.

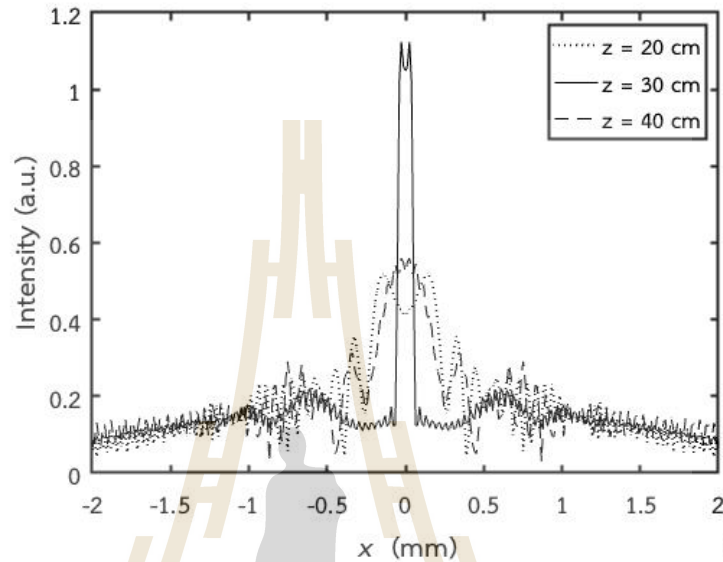


Figure 2.6 Comparisons between the 1D cross-sectional scan of image intensities reconstructed from the hologram of the 100 μm line-shaped particle recorded at the wrong and the correct distance $z = 30$ cm.

In contrast, the correct recording position of 30 cm gives the sharpest reconstruction than the other images. Therefore, the correct particle position can be measured from the reconstructed image.

2.3 Particle Analysis

The interference fringe of the hologram encodes the information of the particle. There are several methods for extracting the information of the particle after the reconstruction process. This section discusses methods for particle analysis.

2.3.1 Particle position

The mean of the reconstructed image intensity is an easy way to use. This approach regards the best-focused reconstruction at the correct distance as having the

highest intensity. The mean values of intensities of reconstructed images of digital holograms \bar{I} is obtained by (Xia, Xu, and Qi, 1999)

$$\bar{I} = \frac{1}{ij} \sum_x^i \sum_y^j I(x, y, z), \quad (2.8)$$

where $I(x, y, z)$ is the image intensity reconstructed at the distance of z . Since its mean intensity is the highest, the particle position can be measured. However, this method is more error-prone, such as when there are many particles or the particles are rotated.

The variance of gray value distribution (VAR) measures the intensity values variation of the reconstructed image, defined as (Qiu, 2017)

$$VAR = \frac{1}{ij} \sum_x^i \sum_y^j \{I(x, y, z) - \bar{I}\}^2, \quad (2.9)$$

The VAR can be used to find the correct reconstruction position. In the case of the particles close to others, the VAR makes an error because it takes into account the mean of the intensity of image. The VAR is good for low particle density, as is the LAP.

Laplace operator (LAP) measures the variation of the intensity gradient of image defined as (Choi and Lee, 2009)

$$LAP = \sum_x^i \sum_y^j \{\nabla^2 I(x, y, z)\}^2, \quad (2.10)$$

where ∇^2 is the discrete Laplacian operator. The LAP can be used for finding the correct reconstruction position by simply choosing the reconstructed image with the highest LAP.

Since the particle image is sharpest at the correct particle location, LAP has better performance when compared with the other two methods because the LAP detects edges of the particle while ignoring other areas with constant intensity gradients (Seo and Lee, 2014).

2.3.2 Particle size

The second analysis is the measurement of the particle size from the reconstructed image at the correct position. After getting the best-focused reconstructed image from the LAP, the particle size measurement is done by scanning the image intensity along the width of the particle at the full width at the half maximum (FWHM) of the normalized intensity.

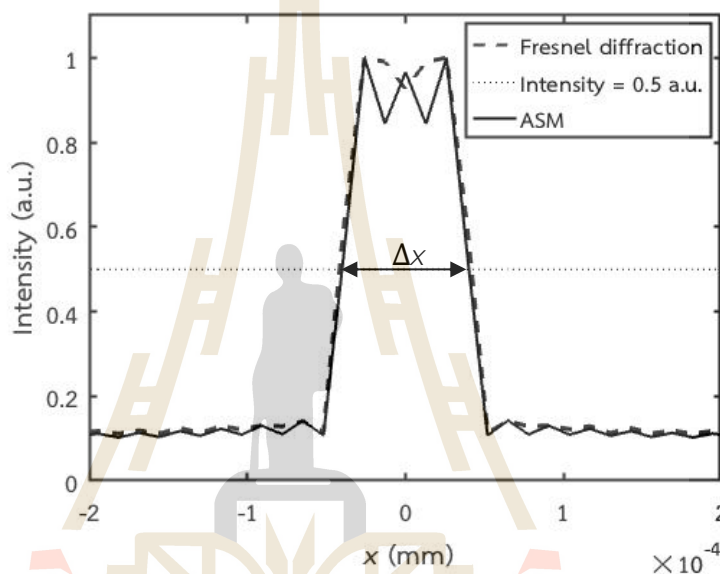


Figure 2.7 Particle size measurement at the FWHM by using the Fresnel diffraction integral and the angular spectrum method.

Figure 2.7 shows the normalized image intensity reconstructed by using the Fresnel diffraction integral (Goodman, 1996) and the angular spectrum method. Their plots are represented by dashed and solid lines, respectively. The dotted line indicates the FWHM, where the particle size is equal to the width of Δx . The FWHM obtained by the two methods is different because the angular spectrum method is not derived by using the Fresnel approximation. The particle size measurement depends on the quality of the sensor, the reconstruction method and the sharpness measurement to find the best-focus from the reconstructed images.

2.3.3 Particle orientation and length

In the analysis of particles with a high aspect ratio, particle orientation and length are considered important parameters. As shown in this flowchart, the conventional method requires many reconstructions to obtain the particle's orientation and length (Khanam et al., 2011).

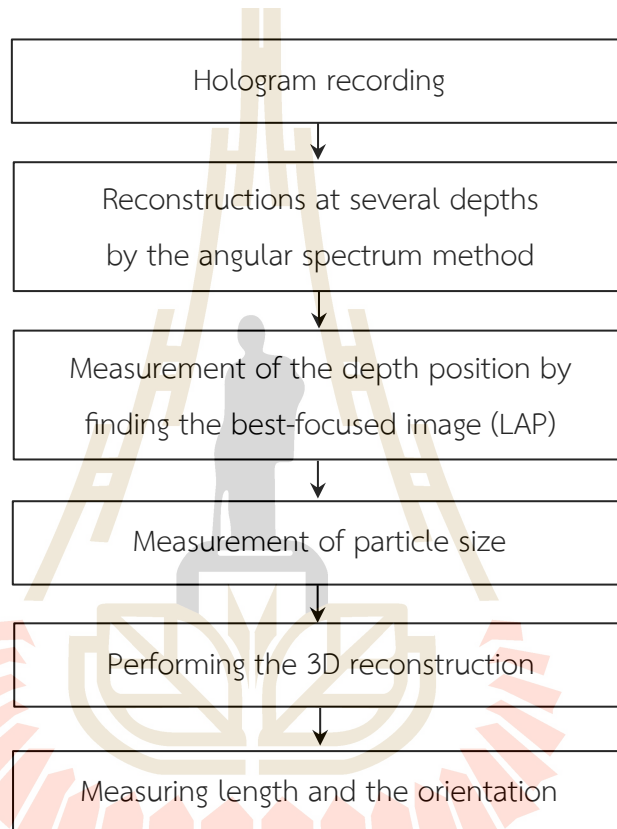
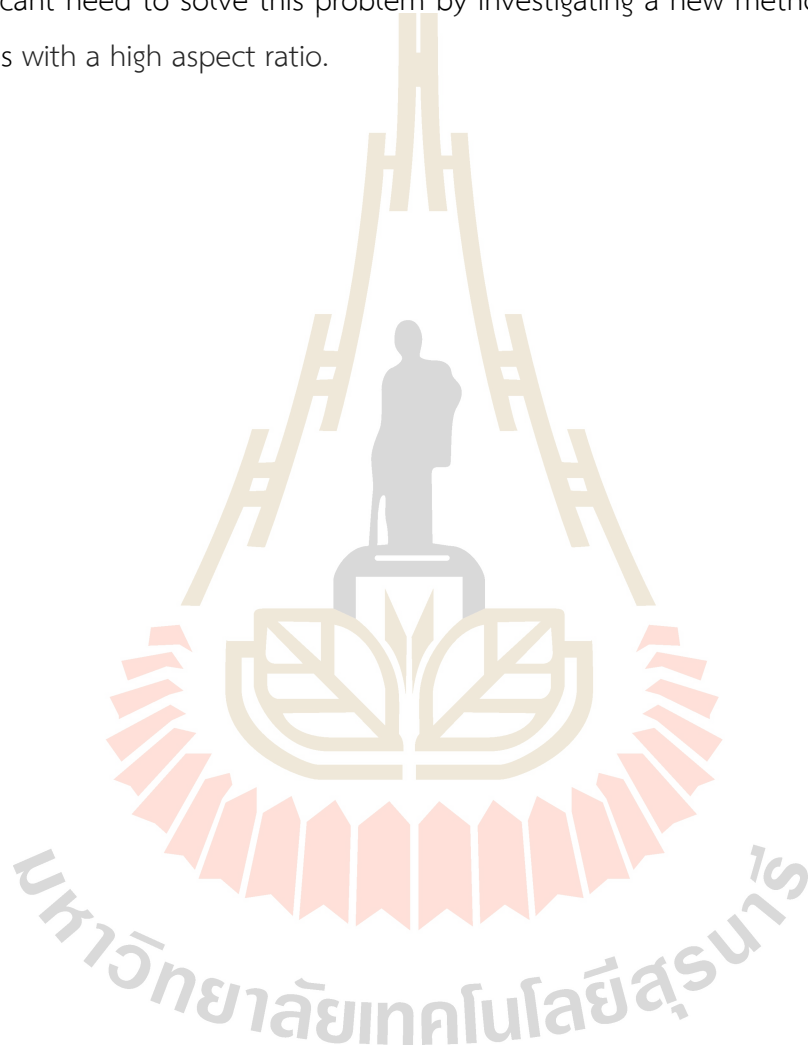


Figure 2.8 Flowchart for particle analysis.

Due to the high aspect ratio, the best reconstruction must be searched from large depth positions by using the LAP. Consequently, the measurements of the particle size need to be done at various depths. The next step is to merge all the best-focused reconstructed images. The merged images give the 3D orientation of the particle.

According to this approach, the particle's orientation can be measured in the range of 0 to 80 degrees (Khanam et al., 2011). The orientation and the range of the depths are then used for finding the particle length. However, it is found that the error

in the length measurement increases as the orientation angle increases due to the limitations of depth of focus and the orientations of particles depend on the selected analytical method. In summary, the particle analysis using the conventional reconstruction methods involves tedious processes because it always requires knowledge of the particle position to obtain the other information. Therefore, there is a significant need to solve this problem by investigating a new method for analyzing particles with a high aspect ratio.



CHAPTER III

WIGNER-VILLE DISTRIBUTION

This chapter presents the principles of a Wigner-Ville distribution (WVD) of in-line hologram analysis of nonstationary signals incident on sensor arrays, specifically the characterization of the WVD for solving the angular spectrum method's problem, representing space-frequency domain information. In the case of a nonstationary signal, the Fourier transform cannot provide space-varying frequency information. This limitation is solved by using the WVD. Using a single coefficient of the Wigner-Ville distribution with minimum amplitude to extract the particle size is proposed. And the last section, the performances for measuring the particle size are proposed.

3.1 Wigner-Ville distribution (WVD)

The Wigner distribution function was proposed to relate the wavefunction in Schrödinger's equation to a probability distribution in phase space by Eugene Wigner in 1932 (Wigner, 1932). The WVD was later developed into nonstationary signal analysis and was applied to signal processing (Ville, 1948).

The WVD of an analytic signal $g(x)$ is defined as (Boashash, 1988)

$$W_I(x, f_x) = \int_{-\infty}^{\infty} g(x + \tau/2)g^*(x - \tau/2)\exp(-j2\pi f_x \tau)d\tau, \quad (3.1)$$

which can be interpreted as the Fourier transform of an instantaneous autocorrelation $g(x + \tau/2)g^*(x - \tau/2)$. In Eq. (3.1), * represents the complex conjugate symbol, while $g(x)$ represents the analytic signal. The analytic signal is defined as,

$$g(x) = s(x) + jH[s(x)], \quad (3.2)$$

where $H[s(x)]$ is the Hilbert transform of the signal $s(x)$ (Abeysekera and Boashash, 1991). The Hilbert transform yields the signal's harmonic conjugate. It shifts the phase of the signal $s(x)$ in the frequency components by +90 degrees. As a result, the analytic signal has only positive spatial-frequency components.

The WVD is a real-valued function. Unlike the short-time Fourier transform, which has a drawback in choosing a suitable width of the analyzing window, the WVD's window is the signal itself. The WVD is the joint space-frequency representation of nonstationary signals (Pachori and Nishad, 2016). Therefore, it is useful for analyzing local frequency variation of hologram's fringes.

3.2 WVD of in-line hologram.

Consider the simulated in-line hologram of the line-shaped particle with a size a of 50 μm recorded with $\lambda = 543.5$ nm at the distance z of 15 cm shown in Figure 2.2(b). Figure 3.1(a) shows the 1-D intensity transmittance plotted along the positive x axis. After generating an analytic signal from the hologram using the function Hilbert transform in Matlab, the WVD of the corresponding signal is calculated by using Eq. (3.1) and is plotted in Figure 3.1(b). The vertical axis of the plot represents the spatial frequency f_x , while the horizontal axis corresponds to the position x . Figure 3.1(b) can be interpreted as showing how the local spatial frequency of the hologram signal varies with respect to position.

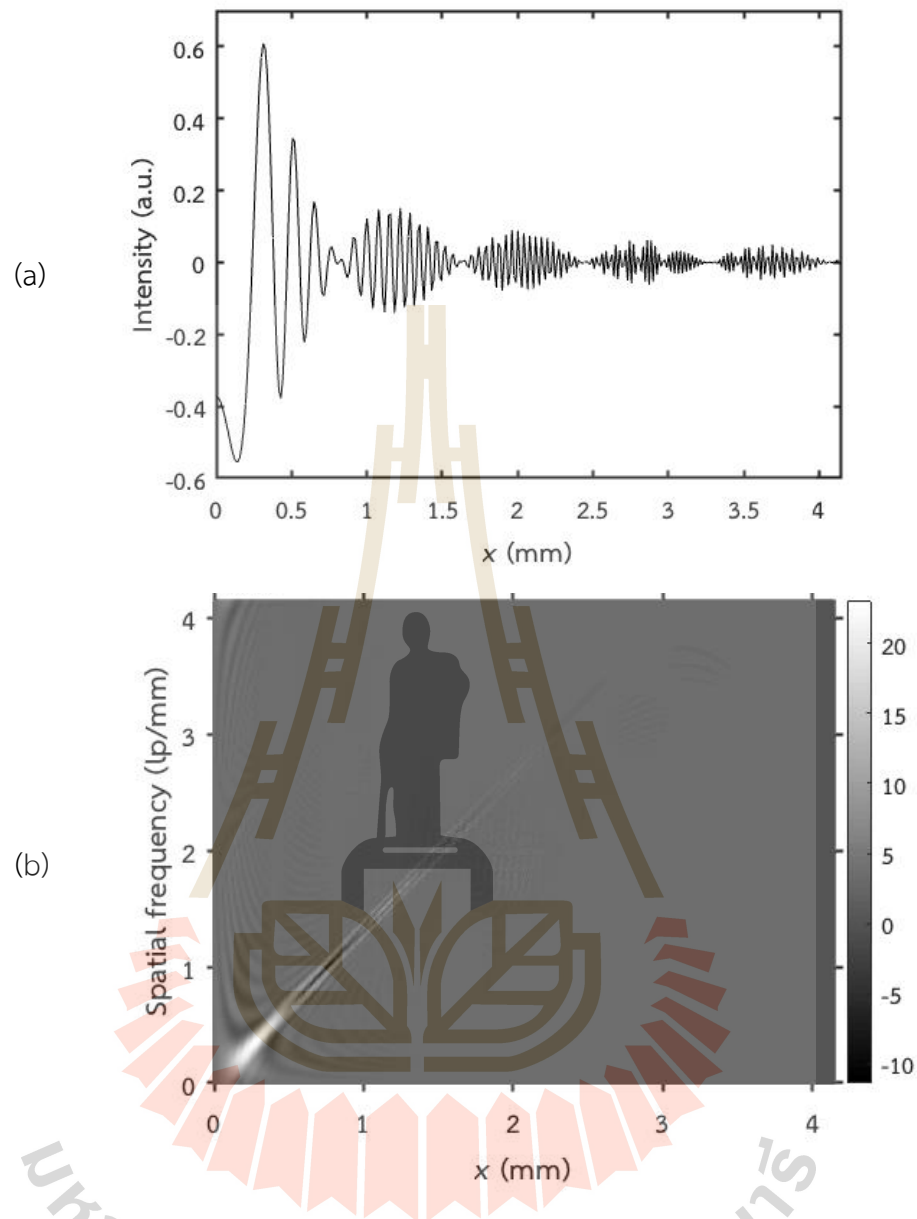


Figure 3.1 (a) The simulated 1-D in-line hologram signal shown in Figure 2.2(b) with a background removal for the positive x axis and (b) the corresponding WVD of the in-line hologram of Figure 3.1(a).

Besides reducing computation time and saving computer storage, this calculation is free from the interference problem because the analytic signal has no negative frequency components. The WVD coefficients with maximum and minimum values are mostly concentrated in a stripe region, whose slope is inversely proportional to the particle position z . When the distance z becomes shorter, the orientation has a

steeper slope. These coefficients relate to the local frequencies of the hologram fringe, which varies linearly with respect to spatial position. Therefore, this characteristic of the WVD signal is in agreement with the properties of the cosine chirp signal given by Eq. (3.3). Furthermore, the particle size affects the width of the stripe area, such that the bigger the particle size, the broader the area.

In order to have a better insight into the WVD coefficient shown in Figure 3.1 (b), the hologram of Eq. (2.1) is simplified by first considering only the second term of Eq. (2.1) along the positive x axis

$$I_a(x) = \cos\left(\frac{\pi x^2}{\lambda z} - \frac{\pi}{4}\right) \left[\frac{\sin\left(\frac{2\pi a x}{\lambda z}\right)}{\frac{2\pi a x}{\lambda z}} \right] \text{rect}\left(\frac{x - L/2}{L}\right). \quad (3.3)$$

This simplification extracts the desired fringe signal. Second, the sinc function is approximated with a product of R cosine functions (Morrison, 1995)

$$\text{sinc}(2f_0 x) = \prod_{n=1}^N \cos\left(\frac{2\pi f_0 x}{2^n}\right), \quad (3.4)$$

where the frequency of the cosine function f_0 equals to $a / \lambda z$. As a result, the analytic expression of Eq. (3.3) could be derived as (Chuamchaitrakool, 2017)

$$g(x) = \sum_{n=1}^{N+1} \left\{ \exp\left[j2\pi f_0 \left(\frac{2n-1}{2^n} x + \frac{\beta x^2}{2f_0} - \frac{1}{2^n f_0} \right) \right] + \exp\left[j2\pi f_0 \left(-\frac{2n-1}{2^n} x + \frac{\beta x^2}{2f_0} - \frac{1}{2^n f_0} \right) \right] \right\} \times \text{rect}\left(\frac{x - L/2}{L}\right). \quad (3.5)$$

with $\beta = 1/\lambda z$. Substitutions of Eq. (3.5) to Eq. (3.1) gives the resultant WVD of the approximated Eq. (3.3) as (Chuamchaitrakool, 2017)

$$W_{I_a}(x, f_x) = \sum_{k=1}^{2^{N+1}-1} \left[\sum_{m=1}^k (-1)^m + \sum_n 2 \cos\left\{ 2\pi f_0 \left[\frac{2^{N+1} - 2(|2^N - l| + 1)}{2^N} \right] x \right\} \right] \times 2(L - 2|x - L/2|) \text{sinc}\left\{ 2(L - 2|x - L/2|) \left(f_x - \left(\frac{2^N - k}{2^N} \right) f_0 - \beta x \right) \right\}, \quad (3.6)$$

where $f_x = x/\lambda z$ is the spatial frequency of the hologram fringe. l is the index of the cosine terms, whose range is determined according to Table 3.1.

Table 3.1 The range of the index of l of cosine terms in Eq. (3.6).

k	l
Even number and $\leq 2^N$	Even number and $l \leq k$
Even number and $> 2^N$	Even number and $l \leq 2^{N+1} - k$
Odd number and $\leq 2^N$	Odd number and $l \leq k$
Odd number and $> 2^N$	Odd number and $l \leq 2^{N+1} - k$

$k = 1, 2, 3, \dots, 2^{N+1} - 1$. The maximum number of the WVD components is equal to $2^{N+1} - 1$. For $N = 5$, there are 63 components of the WVD that appear along the same slope in the WVD plane. In Eq. (3.6), the characteristics of the WVD of the simplified in-line hologram are as follows: First, each component of the WVD is equal to the product of two functions: the spatial cosine function and the 2-D sinc function of the space and the spatial frequency. Second, the sinc function is modulated by the triangular function, whose width is equal to the hologram length. Its spatial frequency is determined by β and f_0 . Therefore, the significant values of the WVD of the in-line hologram appear along a positive slope, as shown in Figure 3.2.

3.2.1 The WVD coefficient with minimum amplitude

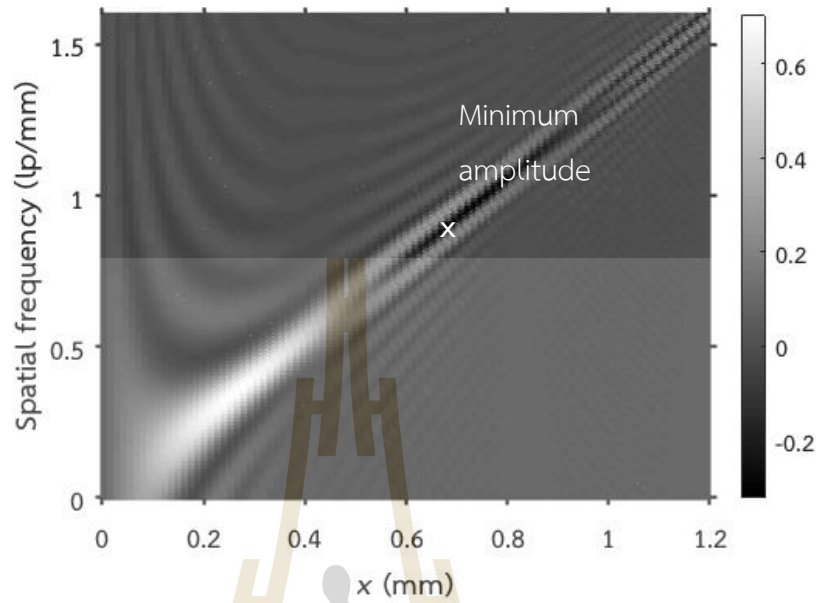


Figure 3.2 Distribution of the WVD coefficients obtained by using Eq. (3.6) with $N = 5$, $2a = 100.00 \mu\text{m}$, $z = 15 \text{ cm}$, and $\lambda = 543.5 \text{ nm}$.

Figure 3.2 is a heat map of the WVD calculated by using Eq. (3.6) for $N = 5$ using the same diameter $2a$, wavelength λ , and distance z as in Figure 3.1(b). As compared to Figure 3.1(b), the significant WVD coefficients appear along the same slope in the WVD plane. There is a single WVD coefficient with the minimum amplitude among the 63 WVD components in the stripe area. When a line is drawn through the minimal coefficient and the origin of the WVD plane, the line crosses the middle of the WVD coefficient stripe. Therefore, this minimal coefficient corresponds to the 32nd component of the WVD, which crosses through the center of the stripe. The 32nd component of the WVD $W_{I_{a32}}$ can be mathematically written as

$$W_{I_{a32}}(x, f_x) = \sum_n 2 \cos \left\{ 2\pi f_0 \left[2 - \frac{2(|2^5 - l| + 1)}{2^4} \right] x \right\} \times 2(L - 2|x - L/2|) \text{sinc}\{2(L - 2|x - L/2|)(f_x - \beta x)\} \quad (3.7)$$

where n is 2, 4, 6, ..., 32. The summation of 16 cosine functions in Eq. (3.7) can be simplified as the product of the cosecant and the sine functions.

$$W_{I_{a32}}(x, f_x) = \csc(\pi f_0 x / 8) \sin(4\pi f_0 x) \\ \times 2(L - 2|x - L/2|) \text{sinc}\{2(L - 2|x - L/2|)[f_x - \beta x]\} \quad (3.8)$$

This cosecant function has a spatial frequency which is 32 times smaller than the frequency of the sine function. As the phase of the cosecant function varies from 0 to π , its amplitude decreases nonlinearly from an undefined value. Therefore, it attenuates the amplitude of the sine function. Since the product of the triangular and the sinc functions in Eq. (3.8) is broader than that of the first two terms, it can be concluded that the minimum WVD coefficient is mainly caused by the sine function of the 32nd component of the WVD. The validity of the analysis can be determined by comparing the WVD coefficient of the hologram signal shown in Figure 3.1(b) and Eq. (3.8). In Figure 3.3, the solid line represents the WVD coefficients scanned along the stripe's center with the origin as the starting point, while the dotted line is the 32nd component of the WVD calculated by using Eq. (3.8). It is apparent that the coefficients with the minimum amplitude appear at the same position.

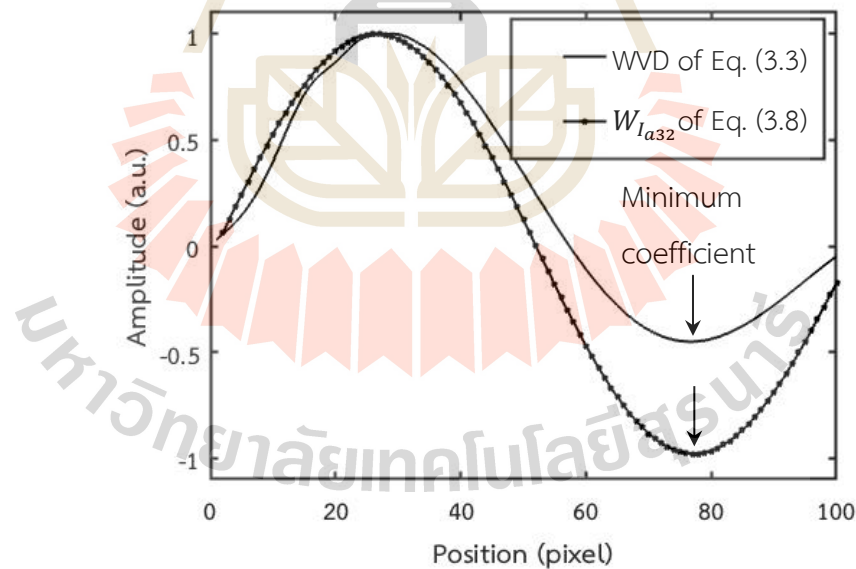


Figure 3.3 Comparison of 1-D plots along the slope of the WVD coefficients of Eqs. (3.8) with WVD of the original hologram in Figure 3.1(b).

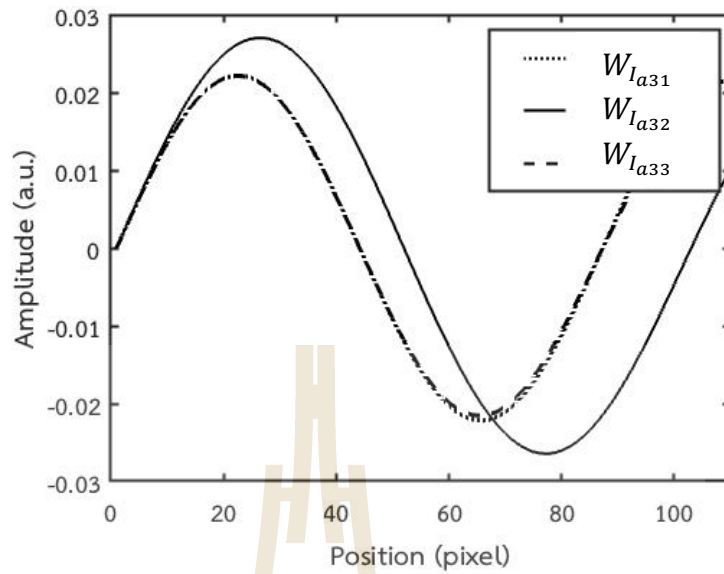


Figure 3.4 1-D plots along the corresponding slope of the 31st, 32nd and 33rd components of WVD.

Figure 3.4 shows amplitude variations of the 31st, 32nd and 33rd components of the WVD scanned along the slope. They are calculated by using Eq. (3.8) and represented by the solid, dashed, and dotted lines, respectively. In comparison with the other two components, the 32nd component has the lowest amplitude. Therefore, it can be concluded that the sinc function of $W_{I_{a32}}$ is truly the origin of the minimum amplitude.

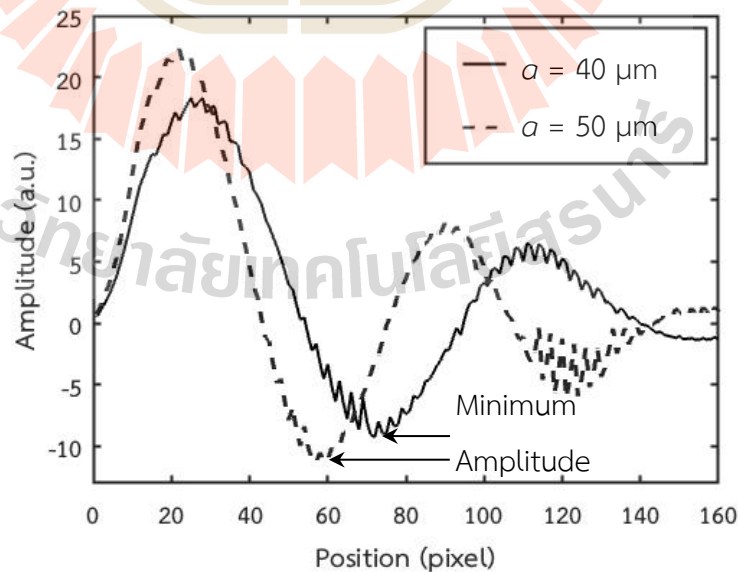


Figure 3.5 Plots of the WVD coefficients scanned along the slopes $1/\lambda z$ for the particle sizes $a = 40$ and $50 \mu\text{m}$, respectively.

Figure 3.5 confirms the dependency of the minimum coefficient position on the particle size. The minimum coefficient of the spatial frequency of the bigger particle diameter is at a lower pixel number than the smaller particle diameter.

3.2.2 Previous WVD-based particle sizing

The WVD-based particle sizing has been reported by Chuamchaitrakool et al. (Chuamchaitrakool, Widjaja and Yoshimura, 2015) using the local frequencies scanned at the half length of the holograms being analyzed. According to Eq. (3.6), for $N = 5$, $W_{I_{a1}}$ and $W_{I_{a63}}$ of the WVD components given by

$$W_{I_{a1}}(x, f_x) = 2(L - 2|x - L/2|) \times \text{sinc}\{2(L - 2|x - L/2|)\{f_x - (62/64)f_0 - \beta x\}\} \quad (3.9)$$

and

$$W_{I_{a63}}(x, f_x) = 2(L - 2|x - L/2|) \times \text{sinc}\{2(L - 2|x - L/2|)\{f_x + (62/64)f_0 - \beta x\}\}. \quad (3.10)$$

Plots of $W_{I_{a1}}$ and $W_{I_{a63}}$ calculated using Eqs. (3.9) and (3.10) appear as the upper most and the lowest signals in Figure 3.6, respectively. The peaks of the two components that always appear at the location at $L/2$ on the WVD plane are higher than the other components, because their amplitudes are modulated only by the triangular functions. Therefore, the peak locations of the $W_{I_{a1}}$ and the $W_{I_{a63}}$ can be easily detected by scanning the WVD output along the frequency axis at the spatial position $L/2$ in Figure 3.6. By substituting $x = L/2$ into Eqs. (3.9) and (3.10), the peak positions of $W_{I_{a1}}$ and the $W_{I_{a63}}$ along the spatial-frequency axis are determined by the particle size as

$$f_x = \pm(62a/64\lambda z) + \beta L/2. \quad (3.11)$$

Consequently, the particle size can be calculated from the spatial-frequency value at the peak by

$$a = \pm \frac{64}{62} \lambda z (f_x - \beta L/2). \quad (3.12)$$

Equation (3.12) reveals that the particle size can be measured, provided the particle position is known.

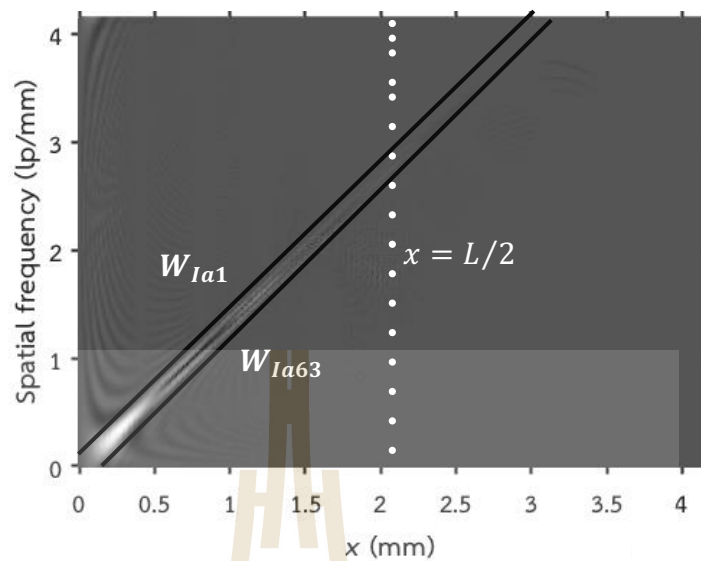


Figure 3.6 The WVD coefficients of the in-line hologram for $z = 15$ cm scanned at $x = L/2$.

The process to extract the particle size using the average of the peak positions of the 1st and the 63th of the WVD components along the spatial frequency axis at $x = L/2$ is summarized in Figure 3.7.

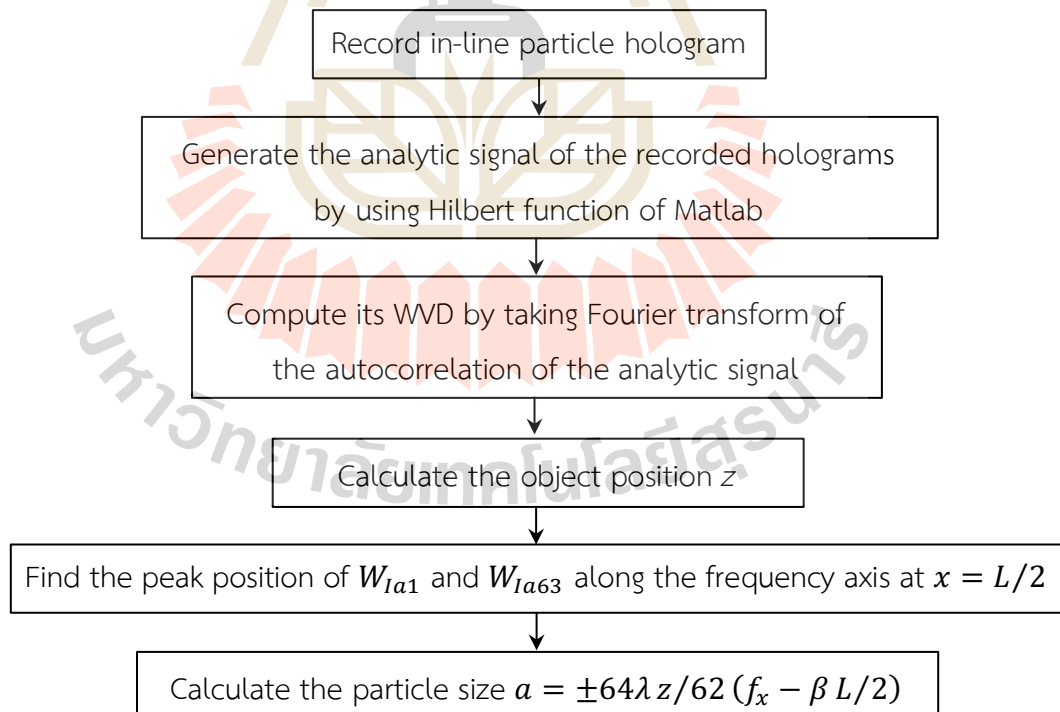


Figure 3.7 Flowchart for the particle size extraction using the peak position of W_{Ia1} and W_{Ia63} along the frequency axis at $x = L/2$.

3.3 Proposed extraction of particle size using a single WVD coefficient with minimum amplitude

According to Eq. (3.8), the coefficient with the minimum amplitude is mainly caused by the sine function of the 32nd component of the WVD. In the x direction, the position of the minimum amplitude is located at the negative peak of the sine function, which is $\frac{3}{4}T$ or

$$\text{Pixel number of } x@min \times \Delta x = \frac{3}{4}T, \quad (3.13)$$

where $x@min$ and Δx are the position of the minimum amplitude coefficient in the x direction and the pixel size of the image sensor, respectively. T represents the period of the sine function in Eq. (3.8) and is defined as

$$T = \frac{1}{2 \times f_0} = \frac{\lambda z}{2a}. \quad (3.14)$$

Substitution of Eq. (3.14) into Eq. (3.13) gives

$$\text{Pixel number of } x@min \times \Delta x = \frac{3\lambda z}{8a} \quad (3.15)$$

or

$$a = \frac{3\lambda z}{8(\text{Pixel number of } x@min \times \Delta x)}. \quad (3.16)$$

Since $f_x = x/\lambda z$, Eq. (3.16) can be rewritten as

$$a = \frac{3}{8 \times \text{Pixel number of } f_x@min \times \Delta f_x}, \quad (3.17)$$

where Δf_x is the spatial frequency resolution of the WVD, given by $1/2L$. Equation (3.17) shows that the relationship between the particle size is inversely proportional to the spatial frequency at the minimum coefficient position. Therefore, the particle size can be measured by detecting the position of the minimum amplitude coefficient in the spatial frequency direction. This is the first significance of this study because the

particle size can be measured without searching the particle position as the conventional numerical reconstructions do. The second one is that the error in size measurement is minimized, because it is free from the error in particle tracking.

The process to extract the size of the particle by using the proposed method of Eq. (3.17) is shown in figure 3.8. This newly proposed method for sizing line-shaped particle has a fast measurement time without sacrificing its accuracy.

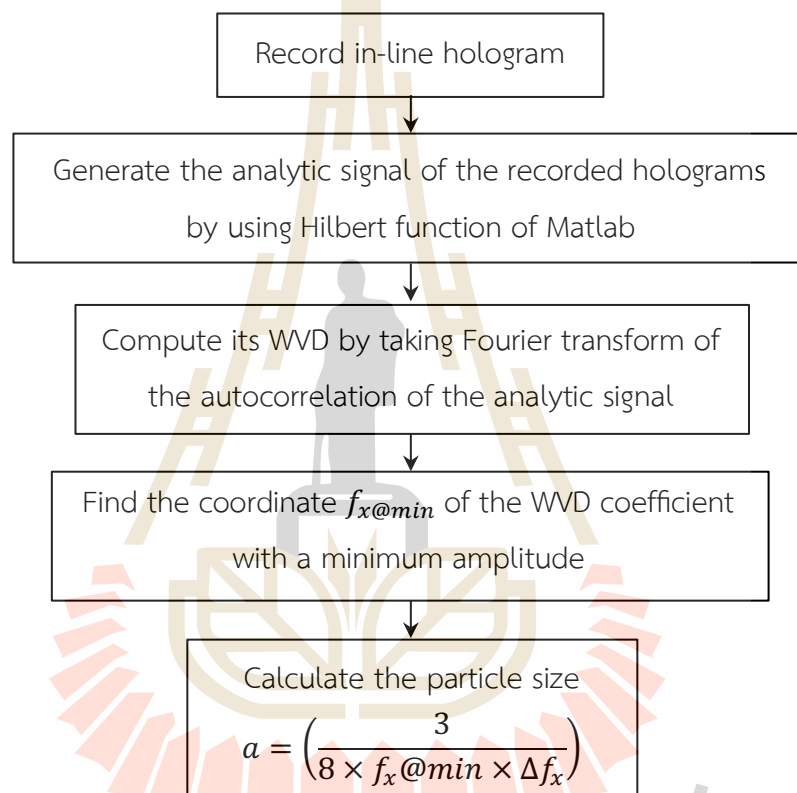


Figure 3.8 Flowchart of the line-shaped particle sizing using the single spatial frequency information of the WVD coefficient with minimum amplitude.

3.4 Particle sizing performance

Consider an implementation of the proposed particle sizing method using the sensor with the resolution of $N \times N$ pixels in an area of $L \times L$, giving the pixel size of $\Delta x = L/N$. The recording of the particle hologram needs to satisfy the Nyquist sampling theorem (Nair, 2002). For the hologram of a line-shaped particle, the hologram frequency has to be smaller than twice the sensor's sampling frequency

$$f \leq \frac{f_{sampling}}{2}. \quad (3.18)$$

The sampling frequency $f_{sampling}$ of the sensor is inversely proportional to the pixel size Δx or

$$f_{sampling} = \frac{N}{L}. \quad (3.19)$$

The preceding discussion shows that the WVD coefficient with the minimum amplitude appears at the negative peak of the sine function in Eq. (3.8), whose frequency can be expressed as

$$f_{sine} = 1/T = \frac{2a}{\lambda z}. \quad (3.20)$$

To correctly detect the position of the minimum amplitude, the sensor's sampling frequency must satisfy the Nyquist theorem

$$\begin{aligned} f_{sine} &\leq f_{sampling}/2 \\ \frac{2a}{\lambda z} &\leq \frac{N}{2L} \\ a_{max} &\leq N\lambda z/4L. \end{aligned} \quad (3.21)$$

Equation (3.21) defines the maximum measurable size of the line-shaped particle using the proposed method.

Furthermore, the position of the minimum amplitude is determined by the sine function as

$$x@min = 3\lambda z/8a. \quad (3.22)$$

It is apparent from Eq. (3.22) that the smaller the particle size, the farther the minimum position moves from the origin of the WVD plane. Hence, the minimum coefficient must appear within the sensor length with a size of L

$$L > 3\lambda z/8a. \quad (3.23)$$

According to Eq. (3.23), the minimum measurable size of the line-shaped particle is defined as

$$a_{min} > 3\lambda z/8L. \quad (3.24)$$

Equations (3.21) and (3.24) define the range of measurable size of the line-shaped particle using this proposed method, ensuring the recorded hologram is not under-sampled.

3.5 Particle tracking using a single WVD coefficient with minimum amplitude

In the previous work, particle tracking using a single WVD coefficient with minimum amplitude has been reported (Widjaja, Dawprateep and Chuamchaitrakool, 2017). Figure 3.9 shows the flowchart for tracking particles from the holograms using the single WVD coefficient with the minimum amplitude. To obtain the depth position of the particle, the spatial frequency of the chirp signal at the minimal coefficient $f_{x@min} = x@min/\lambda z$ is detected and used to calculate the depth position z

$$z = \frac{x@min}{\lambda f_{x@min}} \quad (3.25)$$

Therefore, both space and spatial frequency coordinates, x and f_x , of the WVD plane are needed.

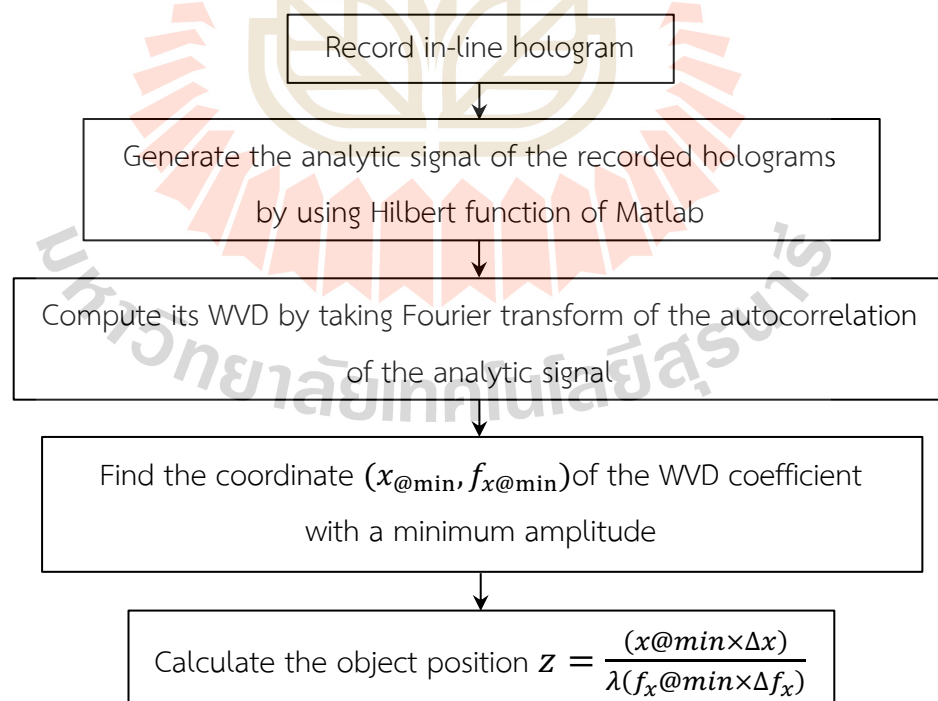


Figure 3.9 A flow chart for extracting the particle position from the in-line hologram with the WVD coefficient with minimum amplitude.

Our previous study (Dawprateep, 2015) shows that the minimum and maximum depth position of the particle that can be measured are defined as

$$z_{min} > \frac{L^2}{\lambda N} \quad (3.26)$$

and

$$z_{max} < \frac{2aL}{\lambda}, \quad (3.27)$$

respectively.

3.6 3D reconstruction of line-shaped particles

In the case of the line-shaped particles, the extracted information of size and position can be used to reconstruct 3-D profile of particles. This section presents the algorithm for reconstructing the 3-D line-shaped particle with arbitrary orientation and length.

Consider the line-shaped particle with a length of p and a diameter of $2a$ is illuminated by the expanded coherent light with a wavelength of λ . The line-shaped particle is oriented at angles α , β , and γ with respect to the x , y , and z axes in 3-D space, respectively, as shown in Figure 3.10. The recorded hologram contains 3-D information about the particle that is confined in a finite 3-D volume with a size of $\delta x \delta y \delta z$ confined by the dotted lines. Here, δx , δy , and δz stand for the projected lengths of the particle in the x , y , and z axes, respectively. The recording plane is separated from the back plane (x', y', z') of the finite volume at a distance of z_0 .

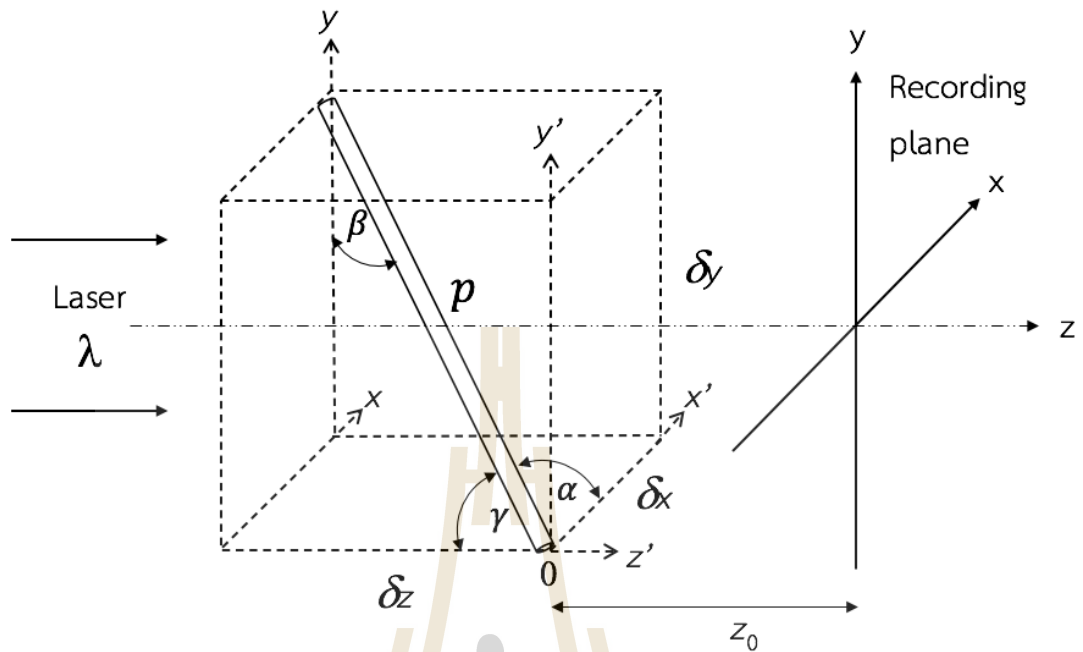


Figure 3.10 Recording geometry of hologram of a line-shaped particle in 3-D space.

From the geometry shown in Figure 3.10, the orientation angles of the particle are mathematically given by

$$\alpha = \arccos\left(\frac{\delta x}{p}\right), \quad (3.28)$$

$$\beta = \arccos\left(\frac{\delta y}{p}\right), \quad (3.29)$$

and

$$\gamma = \arccos\left(\frac{\delta z}{p}\right), \quad (3.30)$$

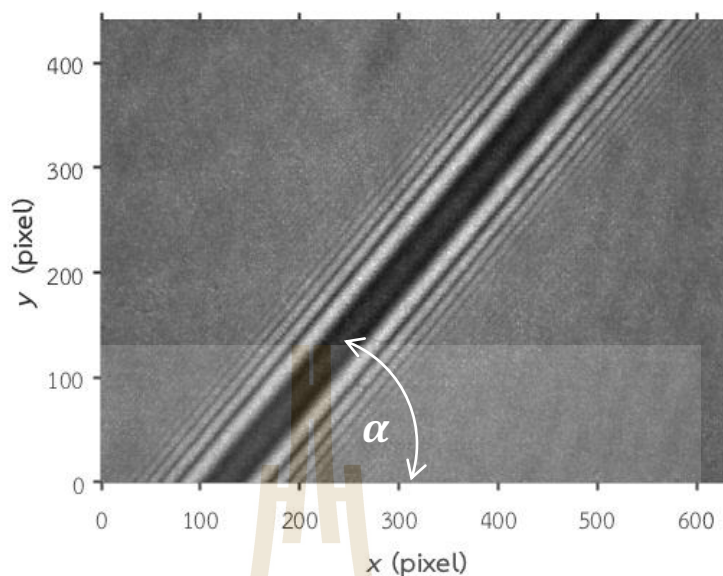


Figure 3.11 The recorded hologram of the line-shaped particle with an arbitrary orientation in 3-D space.

Figure 3.11 shows an example of the recorded hologram of the line-shaped particle with an arbitrary orientation in 3-D space, where the row and column correspond to the vertical and horizontal axes of the recording geometry in Figure 3.10, respectively. It is worth mentioning that the fringe orientation is parallel to the particle length. To reconstruct the 3-D profile particle from this hologram using the proposed WVD, the following process is done:

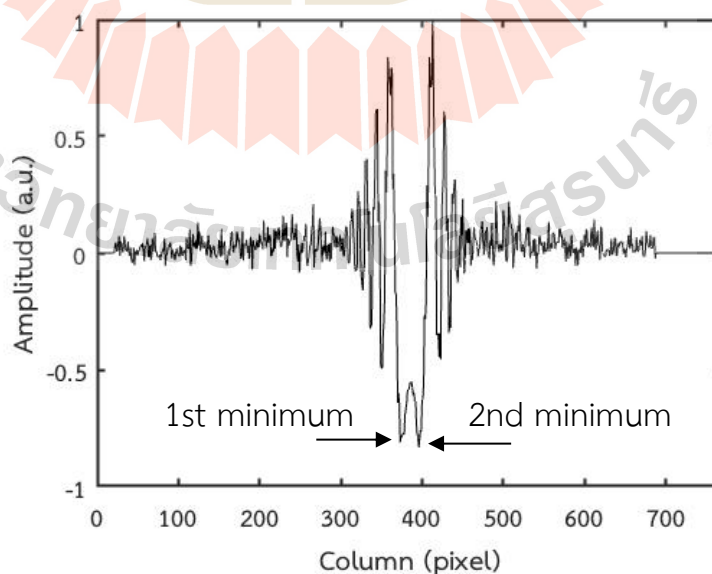


Figure 3.12 1-D cross-sectional scan of the hologram fringe for measuring the angle α .

First, to obtain the angle α , the fringe signal in every row of the hologram in Figure 3.11 is scanned. Figure 3.12 shows the fringe signal scanned at row 350 of the hologram in Figure 3.11. Zeros are added to the left part of the scanned signal because of the limited sensor size. The positions of the first and second minima of the scanned fringe shown in Figure 3.12 are then determined to detect the center of fringe signals. This is because the peaks of the minima are sharper than those of the maxima, yielding accurate peak detection. As a result, the fringe center in each row can be obtained by averaging the minimum positions. Figure 3.13 shows the plot of the resultant averaged positions of the fringe center for all rows. Besides providing the slope of the fringe, the projected length of the particle in the x and y directions can be calculated as the product of the number of columns or rows occupied by the fringe and the pixel sizes, $\delta x = N_{\text{Column}}\Delta x$ and $\delta y = N_{\text{Row}}\Delta y$, respectively. As a result, the particle orientation α with respect to the x axis can be determined as

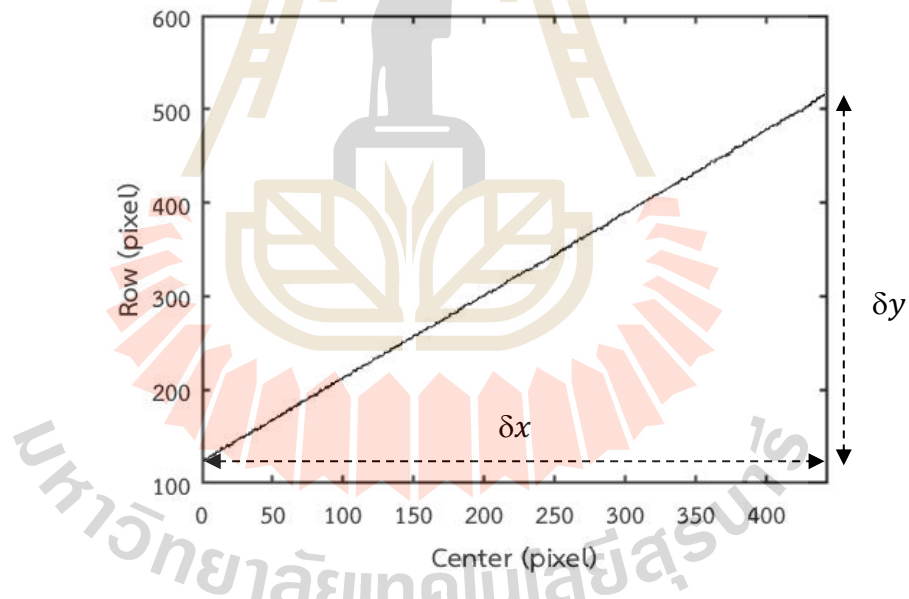


Figure 3.13 Plot of the resultant averaged position of the fringe center as a function of the row.

$$\alpha = \text{atan}(\delta y / \delta x). \quad (3.31)$$

Second, to simplify the extractions of the particle depth and size, the value of the rotation angle α calculated using Eq. (3.31) is used to rotate the hologram back into the vertical direction by the angle $90^\circ - \alpha$ using the Matlab function `imrotate`. This

Matlab function accommodates the dimension of the rotated hologram. The resultant vertically oriented hologram is shown in Figure 3.14. Since it is possible to compute the WVD of the hologram signal along either positive or negative x axis, the particle analysis can be done by using the signals in either the 1st or 2nd area in Figure 3.13. This thesis computes the WVD of the signal along the positive x axis.

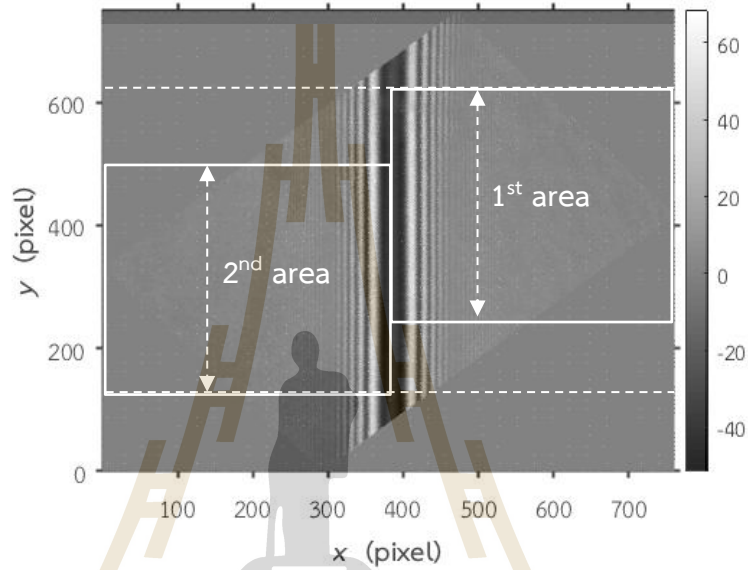


Figure 3.14 The vertically oriented hologram after the rotation with the angle $90^\circ - \alpha$.

Third, the depth of the particle position in each row of the hologram is computed from the scanned fringe using the flowchart shown in Figure 3.9. The difference between the depth at the top of the particle and that at the particle's bottom gives the depth range of δz . Therefore, if the projected particle height δy occupies the range of δz , the rotation angle β can be calculated as

$$\beta = \arctan\left(\frac{\delta z}{\delta y}\right). \quad (3.32)$$

Fourth, the angle γ is calculated using the direction cosines of the particle orientation

$$\cos^2 \gamma = 1 - \cos^2 \alpha - \cos^2 \beta. \quad (3.33)$$

Finally, the particle length p is calculated by using the Pythagoras theorem

$$p = \sqrt{\delta x^2 + \delta y^2 + \delta z^2}. \quad (3.34)$$

The preceding discussion reveals that performance of the 3-D reconstruction of the particle profile is determined by the sensor resolution and the WVD-based particle tracking.

Equation (3.34) can be regarded as the expression for the longest measurable particle length, while the shortest measurable length occurs when the particle occupies 2 pixels along either the sensor's x or y axis. Table 3.1 summarizes the range of measurable size, position, and length of the line-shaped particle from the digital holograms using the proposed WVD.

Table 3.2 Range of the measurable size, position and length of the line-shaped particle from the digital holograms using the proposed WVD.

	Minimum	Maximum
a	$a_{min} > \frac{3\lambda z}{8L}$	$a_{mn} \leq \frac{N\lambda z}{4L}$
z	$z_{min} > \frac{L^2}{\lambda N}$	$z_{max} < \frac{2aL}{\lambda}$
p	$2\Delta x$ or $2\Delta y$	$\sqrt{x_0^2 + y_0^2 + z_0^2}$

The above discussion reveals that performance of the 3-D reconstruction of the particle profile is determined by the sensor resolution and the WVD-based particle tracking. According to Eqs. (3.31), (3.32), and (3.33) and also taking into account the positive and negative directions of the axes, the proposed method can be used to reconstruct the line-shaped particle with an orientation angle that varies from 0 to 180°. Finally, the obtained particle information such as: size, position, orientation and length, can be used to reconstruct the 3D profile of the line-particle.

Figure 3.15 shows the process for plotting 3D particles using the proposed method.

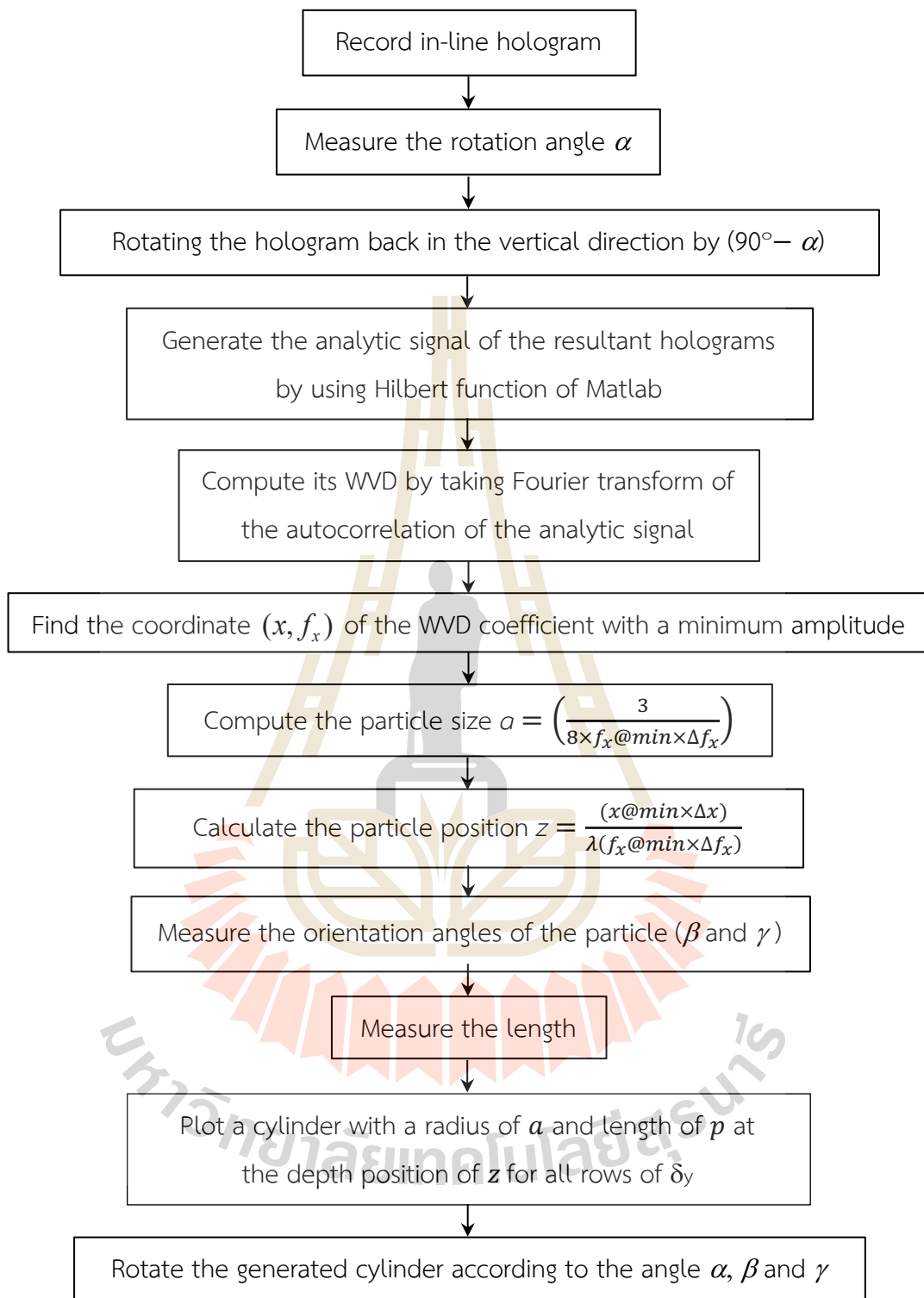


Figure 3.15 A flow chat for plotting 3D profile of particles using the proposed method.

The results of the reconstruction of the 3D particle profile using this proposed method are presented in the next section.

CHAPTER IV

EXPERIMENTAL VERIFICATIONS

First, this chapter discusses the experimental verifications of the proposed particle sizing by using a single spatial frequency of the WVD coefficient with the minimum amplitude. Second, the 3D reconstruction of the line-shaped particle by using the size, position, length, and orientation from the in-line hologram signals is described.

4.1 Experimental setup

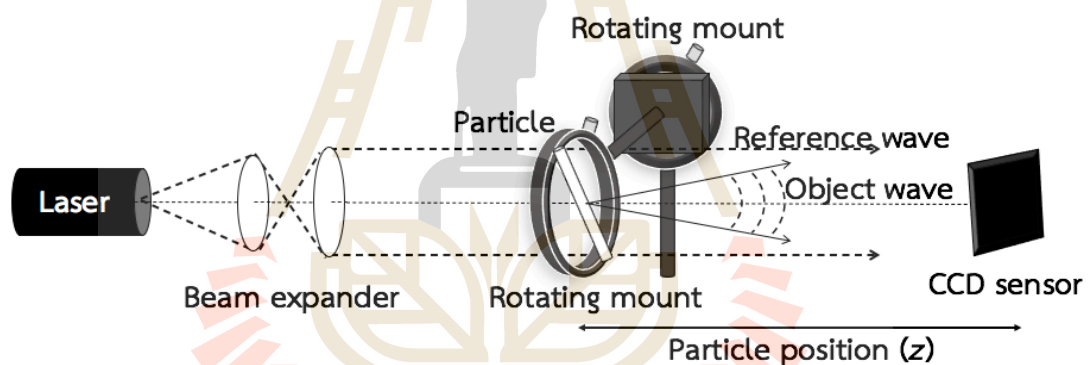


Figure 4.1 A schematic diagram of an optical setup for recording the digital in-line holograms of the microtube with different orientation in 3-D space.

Figure 4.1 shows a schematic diagram of an optical setup for recording the digital inline holograms of polycarbonate microtubes with diameters $2a$ of $80 \mu\text{m}$ and $100 \mu\text{m}$ (Paradigm Optics, CTPC-053-080 and CTPC-067-100). The holograms of the microtubes were experimentally generated by using a He-Ne laser with an operating wavelength λ of 543.5 nm (MellesGriot, 05-LGR-193) at the recording distances of 10 to 15 cm . The laser beam was expanded to about 20 mm in diameter using a combination of a spatial filter and a collimating lens to illuminate the whole length of the microtube. The digital holograms of the microtubes were recorded using a CCD

image sensor (HAMAMATSU C5948) with a total resolution of 640×480 pixels in an area of 8.30×6.40 mm². Therefore, the spatial resolution in the vertical and horizontal directions, Δy and Δx , of the holograms was 12.97 μm . The digital holograms were saved in TIFF format. Matlab software version 2019a, run on a macOS version 10.13.6 was used for all computations.

A combination of two rotating mounts (MellesGriot, 07-HPR-223) was used to provide different orientations of the microtubes in 3-D space. Orientation in the (x,y) plane was done by attaching the microtube to the first rotating mount, as shown in Figure 4.2. This mount was installed on the second rotating mount to provide rotation in the (y,z) plane, as shown in Figure 4.3.

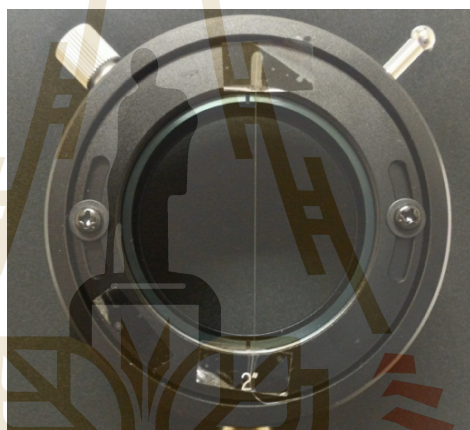


Figure 4.2 A microtube mounted on a rotating mount.



Figure 4.3 A combination of two rotating mounts to rotate the microtube in 3-D space.

Figure 4.4 shows the experimental setup for the verifications of the proposed method and the hologram of the microtube recorded at the distance z away from the sensor and oriented with the angles. It is apparent that the interference fringes are inclined with respect to the x and y axes. The experimental verification of our proposed sizing and reconstruction of the line-shaped particles will be presented in the next section.

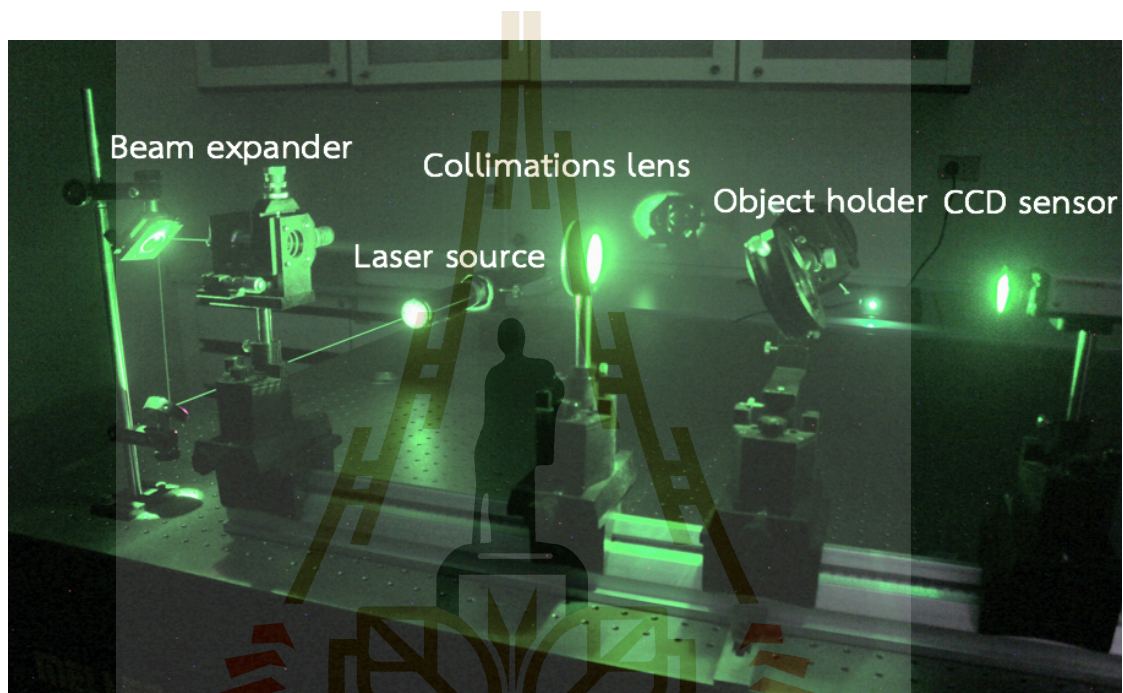


Figure 4.4 Experimental setup for the verifications of the proposed method.

In Table 4.1, the range of measurable particle sizes calculated for recording distances of 10 - 15 cm using Eqs. (3.21) and (3.24) is presented. The measurable particle sizes are determined by the recording distances, the laser wavelength, and the sensor used in the experiment.

Table 4.1 Range of measurable particle sizes using the proposed method for recording distances of 10 - 15 cm.

Recording distance z (cm)	$a_{min} > \frac{3\lambda z}{8L}$ (μm)	$a_{max} \leq \frac{N\lambda z}{4L}$ (mm)
10.0	4.911	1.048
11.0	5.402	1.152
12.0	5.893	1.257
13.0	6.384	1.362
14.0	6.876	1.467
15.0	7.367	1.572

4.2 Experimental verifications of particle sizing from holograms

Figure 4.5(a) shows the recorded in-line holograms of the microtube with diameter is $a = 50 \mu\text{m}$ at the recording distance $z = 15 \text{ cm}$. In order to calculate the WVD of the hologram, the background intensity of the collimated beam shown in Figure 4.5(b) was subtracted from the hologram.

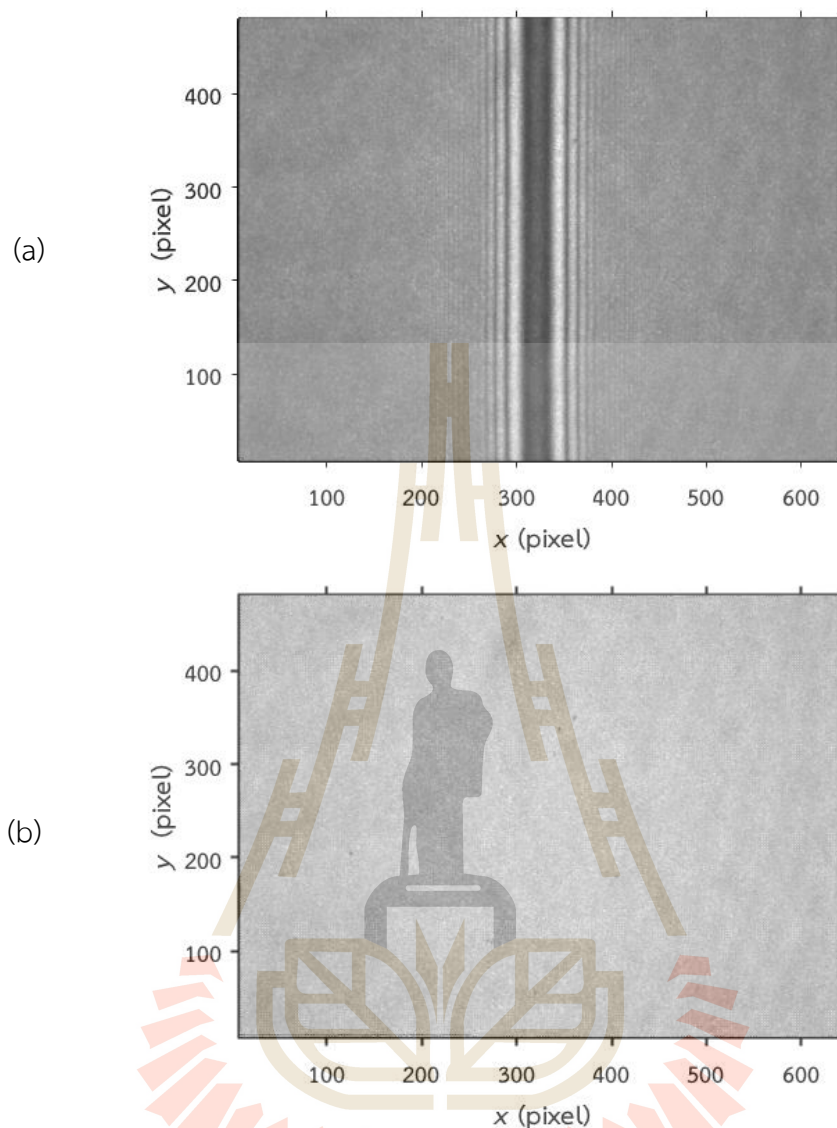


Figure 4.5 (a) The in-line hologram of the 100 μm microtube recorded at the distance $z = 15$ cm with the rotation angles $\alpha = 90^\circ$, $\beta = 0^\circ$ and $\gamma = 90^\circ$ and (b) its background intensity.

Figure 4.6 shows the normalized 1D intensity of the hologram shown in Figure 4.5(a) scanned at the 350th row with background removal. The scanned intensity is compared with the hologram signal simulated using Eq. (2.1). It can be observed from the figure that the background removal almost eliminates the unwanted dc signal.

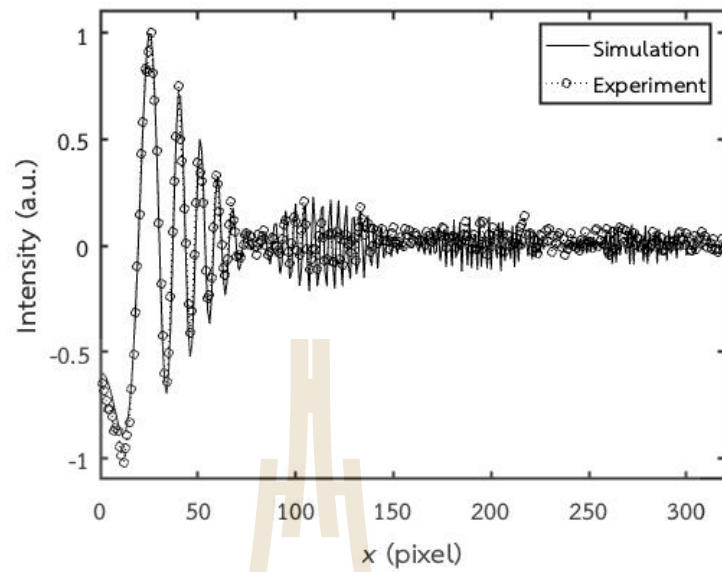


Figure 4.6 Normalized 1D intensity of the recorded particle hologram shown in Figure 4.5(a) and its corresponding simulation with the background removal.

The comparison of the fringe patterns from the simulated and experimental holograms in Figure 4.6 shows that they are almost identical. Thus, the experimental setup could record faithfully the particle holograms.

Figures 4.7(a) and (b) show the WVDs of the holograms of the 80 and 100 μm microtubes recorded at the distance $z = 15$ cm, respectively. Since the particle depth positions are the same, the resultant WVD coefficients with maximum amplitudes appear at the same slope $1/\lambda z$. However, according to Eq. (3.22), the position of the minimum coefficient is dependent on the particle size.

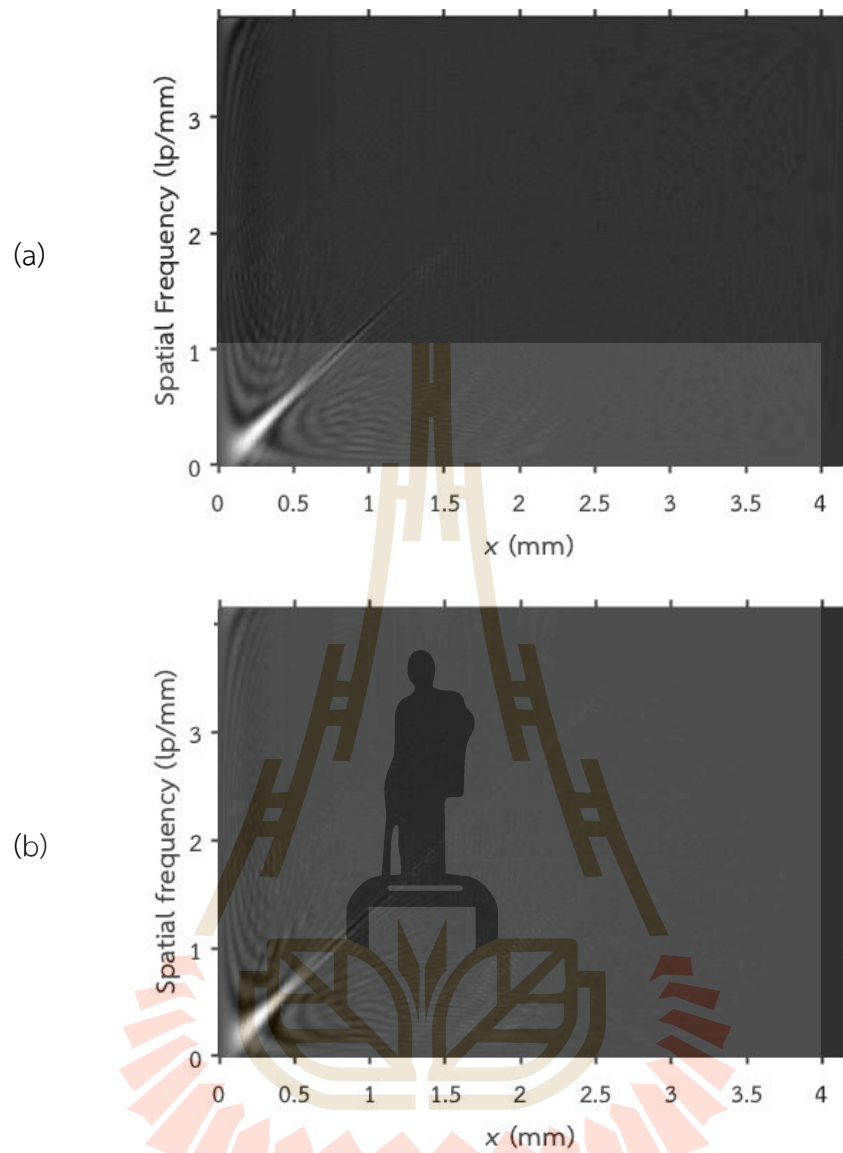


Figure 4.7 The WVD outputs of the holograms recorded at the axial distance $z = 15$ cm. The particle diameters are (a) 80 and (b) 100 μm , respectively.

Figure 4.8 confirms the dependency of the minimum coefficient position on the particle size because the minimum position for the larger particle diameter is at a lower pixel number than that of the smaller one.

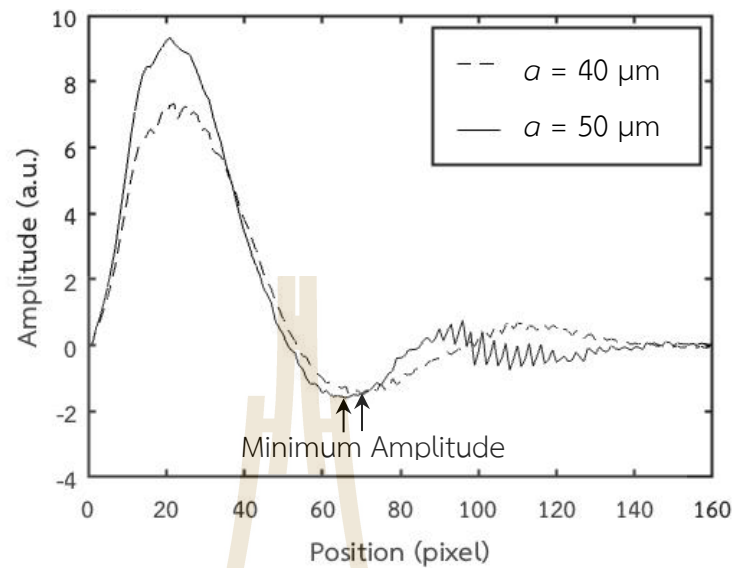


Figure 4.8 Plots of the WVD coefficients scanned along the slopes $1/\lambda z$ of Figure 4.7 (a) and (b).

Table 4.2 Mean of the detected spatial frequencies of the minimum WVD coefficient and the mean absolute errors (MAEs) in the size measurement of microtube with the diameter $2a = 80 \mu\text{m}$ and the rotation angles $\alpha = 90^\circ$, $\beta = 0^\circ$ and $\gamma = 90^\circ$ in the x-y plane by using the proposed single WVD coefficient.

Recording distance z cm	Mean of spatial frequency $f_{x@min}$		Mean of radius a μm	MAE of radius a %
	pixel	lp/mm		
10.0	90.51	10.905	39.99	0.704
11.0	90.51	10.905	39.99	0.694
12.0	90.65	10.921	39.93	0.683
13.0	90.19	10.867	40.14	0.675
14.0	90.13	10.858	40.17	0.654
15.0	90.89	10.951	39.83	0.623

Tables 4.2 and 4.3 present the mean absolute error in the size measurement of the microtubes with the diameters of $2a = 80 \mu\text{m}$ and $100 \mu\text{m}$ from 50 rows, row numbers

325–375, of the experimental holograms, respectively. In the first experimental verifications, the microtubes were oriented in the vertical directions, in the x-y plane.

The errors in the size measurement are always smaller than 1%. The highest error is 0.704% at the shortest position $z = 10$ cm. The experimental results show that the tendency of the errors in the size measurement is inversely proportional to the depth position z of the particle. This is because at the longer depth position, the holograms are less affected by the undersampling effect.

Table 4.3 Mean of the detected spatial frequencies of the minimum WVD coefficient and the mean absolute errors (MAEs) in the size measurement the microtube with the diameter $2a = 100$ μm and the rotation angles $\alpha = 90^\circ$, $\beta = 0^\circ$ and $\gamma = 90^\circ$ in the x-y plane by using the proposed single WVD coefficient.

Recording distance z cm	Mean of spatial frequency $f_{x@min}$		Mean of radius a μm	MAE of radius a %
	pixel	lp/mm		
10.0	89.22	10.749	49.88	0.531
11.0	89.30	10.759	49.84	0.510
12.0	89.06	10.730	49.97	0.498
13.0	87.20	10.506	48.79	0.489
14.0	88.78	10.696	50.16	0.403
15.0	89.29	10.758	49.87	0.353

Table 4.3 shows the errors in the size measurement of the 100 μm microtube have a similar dependency on the depth position of the particles as Table 4.2. However, their values are smaller than those in Table 4.2. This maybe caused by the fact that the fringe intensity modulation given by Eq. (2.1) is proportional to the particle size; the bigger diameter, the higher the modulation. Consequently, the holograms of the smaller microtube has a broader lobe width and a lower intensity transmittance. Since, the fringe signal around the zero-crossing lobe cannot be faithfully sampled

during the hologram recording, the frequency variation of the fringe signal is affected. As a result, the frequency at the minimum amplitude position deviates (Dawprateep and Widjaja, 2021). In summary, the experimental results of the microtube sizing verify that high measurement accuracy can be obtained using the proposed method without searching the depth position of the particle.

4.2.1 Experimental verifications of the particle sizing using the flip and replication technique (FRT).

FRT was introduced in order to improve the spatial frequency resolution by Chuamchaitrakool in 2018 (Chuamchaitrakool, Widjaja and Yoshimura, 2018). The FRT is implemented by flipping and replicating the original hologram signal. The replicated signal is then successively connected to the original one. Besides extending the length of the hologram signal, the successive extensions prevent signal discontinuities. The use of one-time FRT extends the hologram signal twice, reducing the spatial frequency by half. The result of using FRT is shown in Table 4.4.

Table 4.4 Mean of the detected spatial frequencies of the minimum WVD coefficient and the mean absolute errors (MAEs) in the size measurement of the microtube with the diameter $2a = 80 \mu\text{m}$ and $100 \mu\text{m}$ and the rotation angles $\alpha = 90^\circ$, $\beta = 0^\circ$ and $\gamma = 90^\circ$ by using the FRT one time.

Recording distance z cm	Mean of spatial frequency $f_{x@min}$		MAEs of radius a	
	$2a = 80 \mu\text{m}$	$2a = 100 \mu\text{m}$	$2a = 80 \mu\text{m}$	$2a = 100 \mu\text{m}$
	lp/mm	lp/mm	%	%
10.00	11.25	10.18	0.487	0.478
11.00	11.29	10.17	0.449	0.439
12.00	11.29	10.23	0.427	0.417
13.00	11.27	10.22	0.397	0.389
14.00	11.28	10.18	0.373	0.369
15.00	11.28	10.18	0.333	0.311

Table 4.4 shows the average of the size measurements of diameter $2a = 80$ and $100 \mu\text{m}$ from the hologram using the FRT one time, respectively. The average error in measurement of the microtube size by using the FRT reduces as the recording distance increases. Therefore, the FRT could improve the accuracy of the particle size measurement using the proposed method without searching for the particle's depth position.

4.2.2 Experimental verifications of the size measurement from the in-line hologram of rotated particles

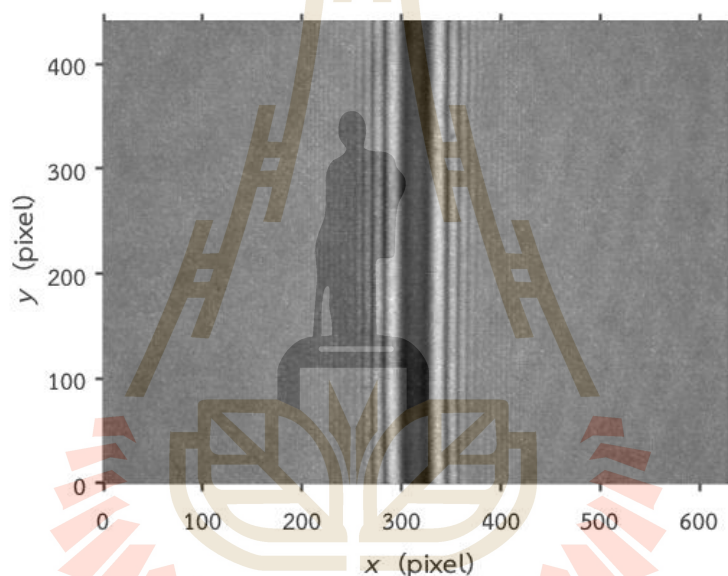


Figure 4.9 The hologram of the $100 \mu\text{m}$ microtube oriented parallel to the yz plane with the angle $\alpha = 90^\circ$, $\beta = 60^\circ$ and $\gamma = 30^\circ$, and the recording distance $z = 14 \text{ cm}$.

Further experimental verifications were done by measuring the size of the $100 \mu\text{m}$ microtubes aligned parallel the yz plane of the schematic diagram of the geometry shown in Figure 3.9 with the angles γ set at about 60° . The holograms were recorded at the recording distance $z = 13, 14$ and 15 cm . All distances were measured from the microtube's center, corresponding to row number 250, to the recording plane. Figure 4.9 shows the hologram of the microtube recorded at the distance $z = 14 \text{ cm}$. Since the microtube is parallel to the y axis, there is no need to rotate the hologram back into the vertical direction. When the orientation angles of the microtube were

calculated from the fringe pattern using Eqs. (3.31) - (3.33), the resultant calculations gave the angles were $\alpha = 90^\circ$, $\beta = 60^\circ$, and $\gamma = 30^\circ$.

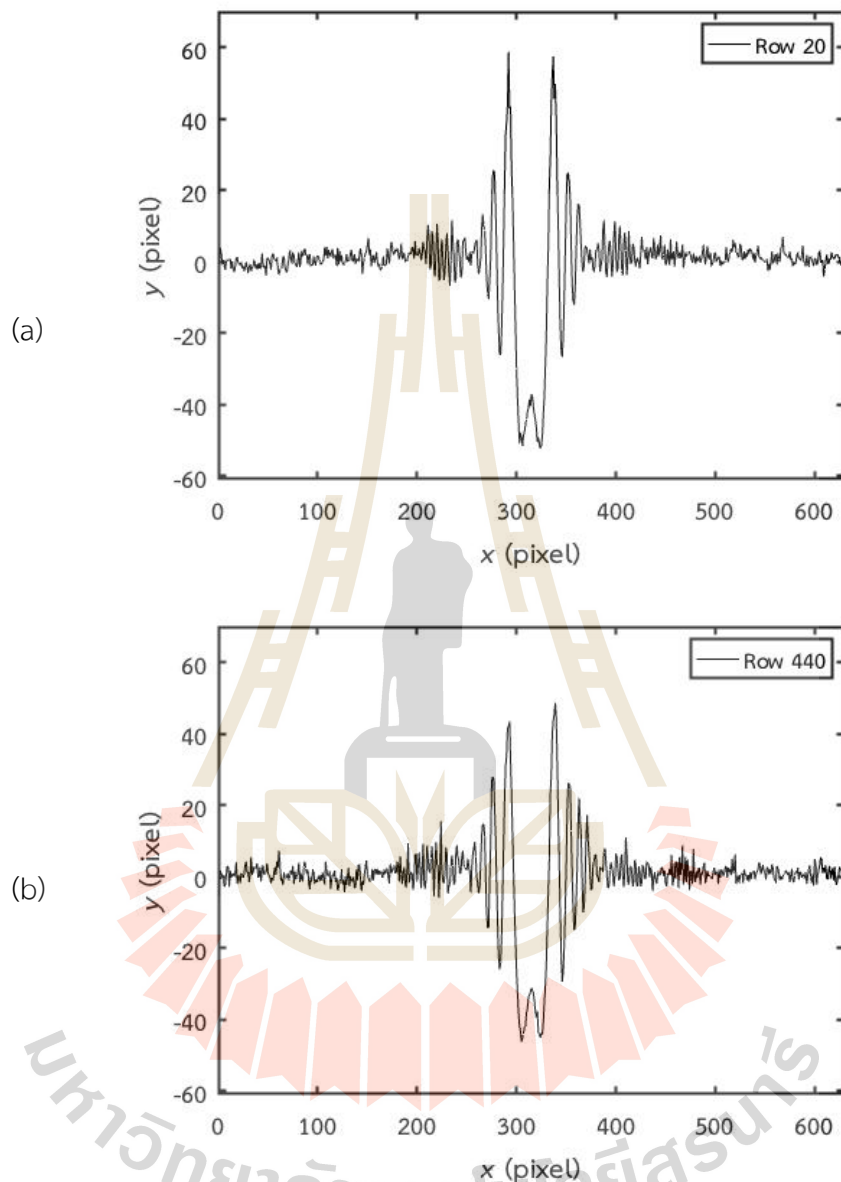


Figure 4.10 1D cross-sectional intensities of the hologram in Figure 4.9, which were scanned along (a) the 20th and (b) the 440th rows, respectively.

Figure 4.10(a) and (b) show the 1D cross-sectional intensities of the hologram scanned along the 20th and the 440th rows of the CCD sensor, respectively. Computations of the WVD of the 1D cross-sectional intensities in Figures 4.10(a) and (b) gave different slopes $1/\lambda z$. The slope of the hologram signal at row 20 is 1.45, while that at row 440 is 1.39. The higher slope means that its local frequency varies faster.

This is because the signal in row 20 is interference from the bottom end of the microtube, which is closer to the recording plane than the top end. Since there are different depth positions along the microtube length, it is important to measure not only the microtube's diameter but also the distance z in each row of the holograms. The region of interest was the rows from 225 to 275, the same row numbers analyzed in the holograms of the vertically oriented microtube. Equations (3.17) and (3.25) were used to calculate the diameter and depth position of the microtube, respectively.

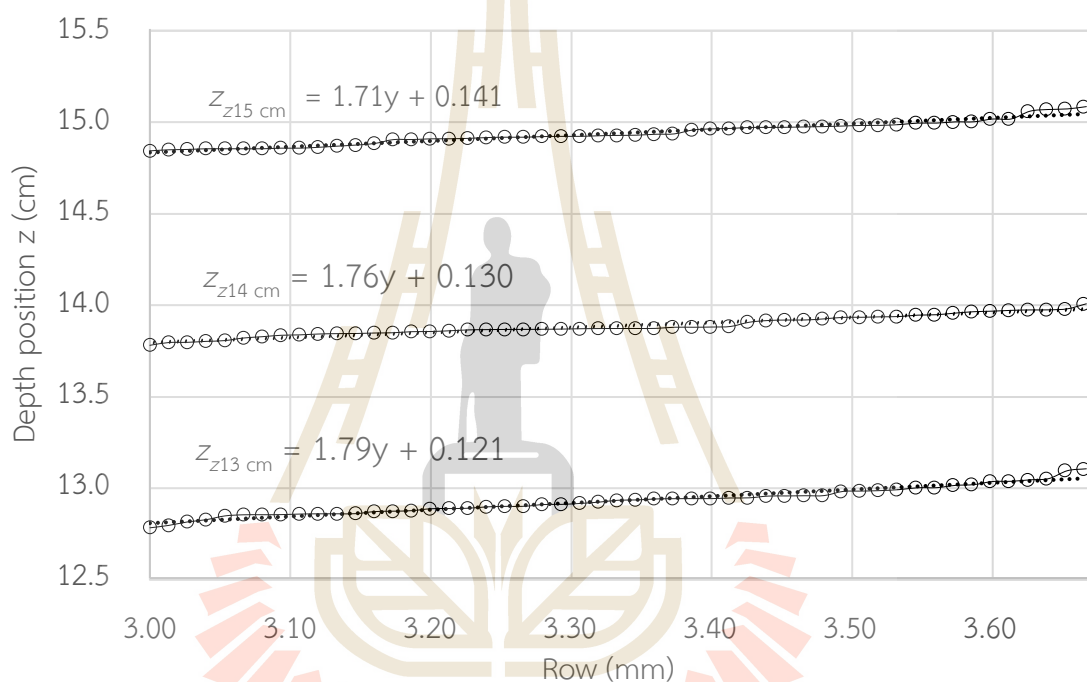


Figure 4.11 Plots of the measured depth position z for different recording distances of the holograms of the microtube parallel to the yz plane as a function of the row numbers represented in mm unit.

Figure 4.11 shows the measured depth position z of the microtube for different recording distances as a function of the rows. The measured position values become longer as the row increases from increases from 225 to 275, equivalent to 3.00 to 3.60 mm, regardless of the recording distances. This agrees with the microtube orientation during hologram recording where row = 3.00 mm is closer to the recording plane than row = 3.60 mm. Consequently, for small row numbers, nonlinear variations of the

measured depth positions are caused by the under-sampled fringe signals. The strong under-sampling effect is apparent for the recording distance of 13 cm.

The errors in the depth and size measurements of the microtube parallel to the yz plane are presented in Table 4.5. The table shows that both the errors in the position and size measurements decrease as the recording distance becomes longer. The errors in the size measurement of the rotated microtube are higher than those without rotations presented in Tables 4.2 and 4.3 because the hologram signal with a short recording distance has a higher chirp frequency than the longer recording distance. When the effect of the undersampling on the holograms is stronger, the frequency of the chirp signal deviates more. Consequently, the MAEs became higher than the previous measurements.

The rotation angle β is calculated by using Eq. (3.32), which can be obtained by applying a linear regression to the plots of the depth positions shown in Figure 4.11. The regression line equation for each plot in Figure 4.11 describes the relationship between the mean of depth position z of the microtube and the rows of the CCD sensor. For example, when the recording distance is 14 cm, the regression line has a slope $\delta z/\delta y$ of 1.76. According to Eq. (3.32), the corresponding angle β is given by $\arctan(\delta z/\delta y)$, which equals 60.4° . The difference between the theoretical and calculated angles may be caused by an error in the alignment of the rotating mounts.

Table 4.5 Errors in measurement of the depth z and the size a from the recorded holograms of the microtube parallel to the yz plane at the angles $\alpha = 90^\circ$, $\beta = 60^\circ$ and $\gamma = 30^\circ$.

Recording distance (cm)	Mean of distance z (cm)	MAE of distance z (%)	Mean of radius a (μm)	MAE of radius a (%)
13.0	12.92	4.514	50.30	3.128
14.0	13.88	4.155	50.49	2.429
15.0	14.94	3.881	50.39	2.391

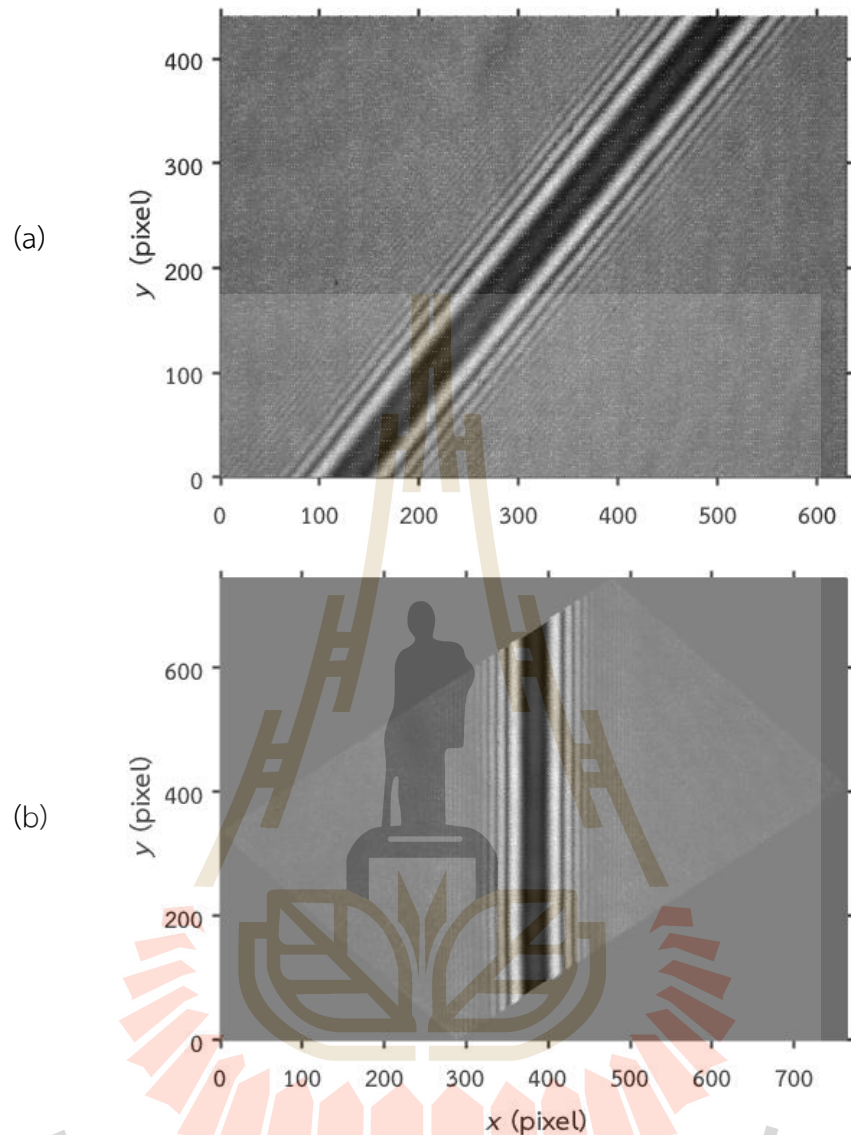


Figure 4.12 (a) The hologram of the microtube oriented parallel to the xy plane with the angle $\alpha = 50^\circ$, $\beta = 40^\circ$ and $\gamma = 90^\circ$ at the recording distance $z = 14$ cm. (b) The vertically oriented hologram after the rotation with the angle $90^\circ - \alpha$.

The next experimental verification was done by recording the microtube oriented parallel to the xz plane with the angles $\alpha = 50^\circ$, $\beta = 40^\circ$, and $\gamma = 90^\circ$. The holograms were recorded at the same recording distances $z = 13, 14$ and 15 cm. The recorded hologram at the distance $z = 14$ cm is shown in Figure 4.12(a). Calculation of the angle

α according to the proposed method discussed in Sect. 3.6 gave a result equal to 50° . Figure 4.13(b) is the resultant hologram rotated back by $90^\circ - \alpha$.

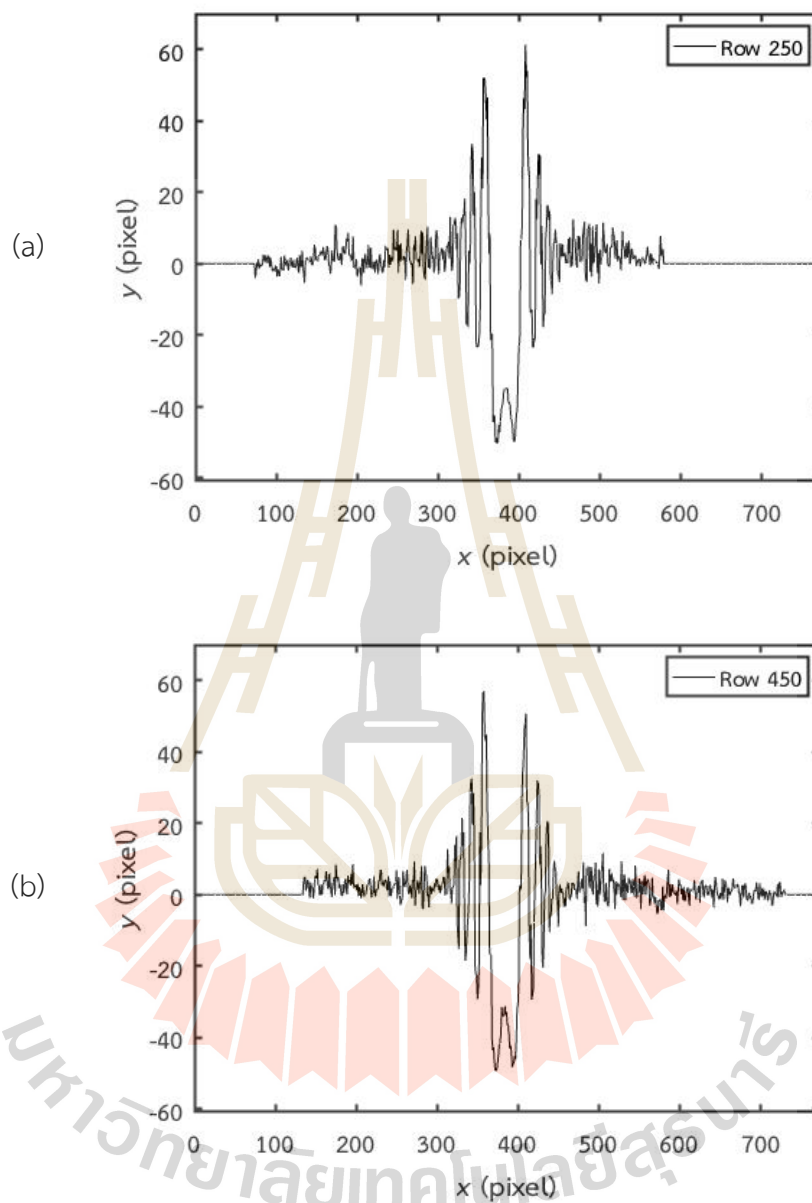


Figure 4.13 1D cross-sectional intensities of the hologram shown in Figure 4.12(b), which were scanned along (a) the 250th and (b) the 450th rows, respectively.

Figure 4.13(a) and (b) show the 1D cross-sectional intensities of the hologram scanned along the 250th and (b) the 450th rows, respectively. The two scanned intensities almost have the same frequency spacings because the microtube is parallel

to the xz plane. Confirmations are done by calculating the slopes of the WVD coefficients. The resultant two slopes have the same value of about 1.40.

Table 4.6 MAEs in the position and size measurements of the 100 μm microtube oriented parallel to the xz plane at the angles $\alpha = 50^\circ$, $\beta = 40^\circ$ and $\gamma = 90^\circ$ using the proposed single WVD coefficient.

Recording distance z (cm)	Mean of distance z (cm)	MAE of distance z (%)	Mean of radius a (μm)	MAE of radius a (%)
13.0	12.95	4.273	47.73	4.170
14.0	13.99	4.144	51.55	4.150
15.0	14.96	3.855	51.14	3.737

Table 4.6 presents the errors in the depth and size measurements of the microtube parallel to the xz plane. The recording distance strongly determines the accuracy in the measurements using the proposed method. The error in the position measurements is slightly lower than those in Table 4.5 because the microtube orientation is parallel to the xz plane. In contrast, it is apparent that the errors in the size measurement are higher than those in Table 4.5. Firstly, this may be caused by the fact that the rotated fringe patterns are sampled at a lower sampling resolution than the vertically oriented patterns. Secondly, since the used CCD sensor has a finite dimension, the rotated hologram signals have a shorter length. Note that the frequency resolution is determined by the signal length. Therefore, degradation of the holograms of the rotated microtube is more significant.

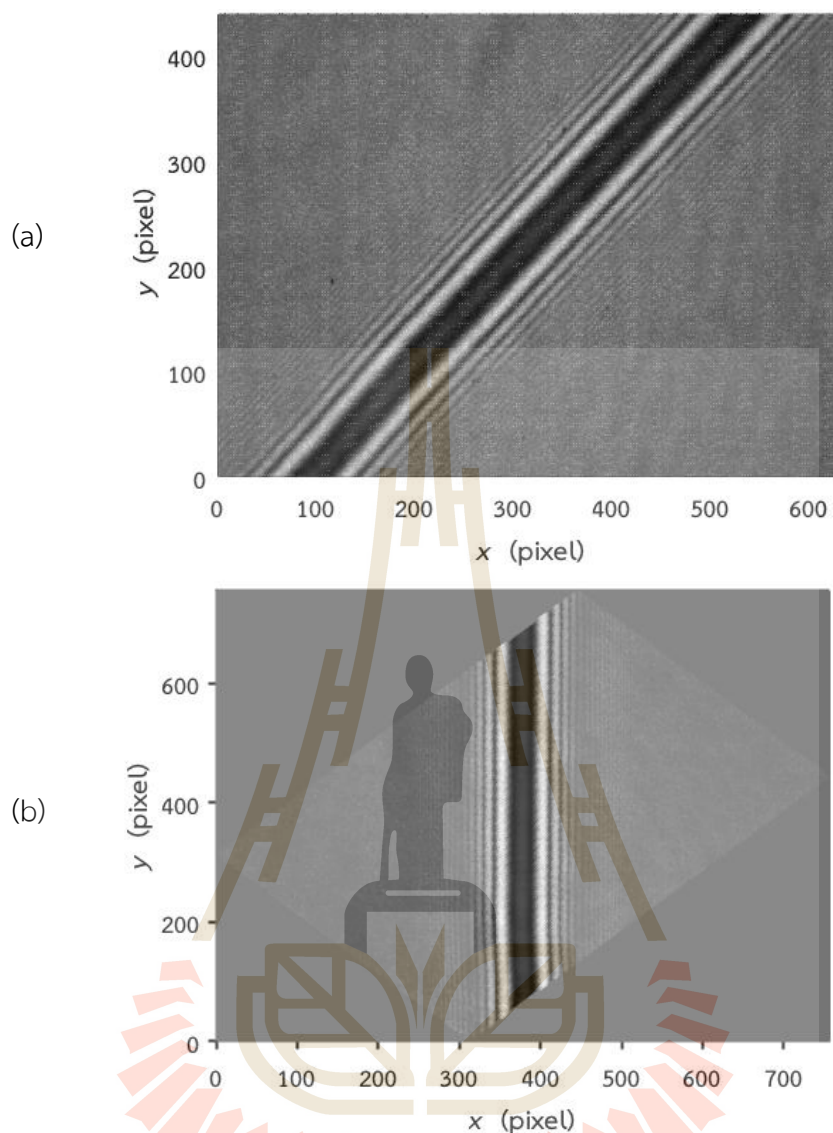


Figure 4.14 (a) The hologram of the 100 μm microtube diagonally oriented in 3D space with the angles $\alpha = 45^\circ$, $\beta = 60^\circ$, and $\gamma = 60^\circ$, and the recording distance $z = 14$ cm. (b) The vertically oriented hologram after the rotation with the angle $90^\circ - \alpha$.

The last experimental verification was done by recording the 100 μm microtube oriented in 3D space in such a way that one end of the microtube was on the origin and the other one crossed the y axis of the schematic diagram of the geometry shown in Figure 3.9. Figure 4.14(a) shows the hologram of the microtube recorded at the distance $z = 14$ cm, while Figure 4.14(b) is the hologram rotated by the angle $90^\circ - \alpha$. The calculations of the orientation angles using the proposed method discussed in Sect. 3.6 gave the angles $\alpha = 45^\circ$, $\beta = 60^\circ$, and $\gamma = 60^\circ$.

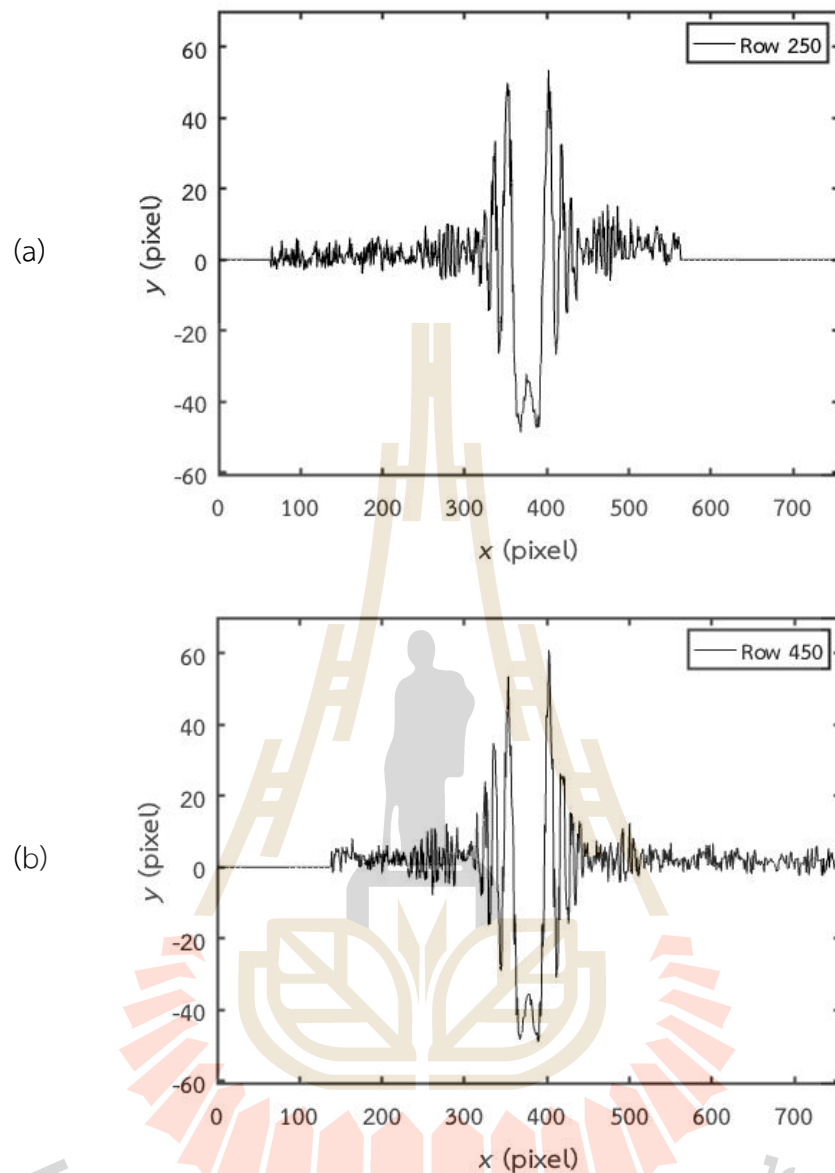


Figure 4.15 1D cross-sectional intensities of the hologram in Figure 4.14(b), which scanned along (a) the 250th and (b) the 450th rows, respectively.

Figures 4.15(a) and (b) show the 1D cross-sectional intensities of the hologram shown in Figure 4.12(b). They were scanned along (a) the 250th and (b) the 450th rows, respectively. The scanned fringe signals reveal that they appear as a flipped signal with respect to the y axis and the difference between the fringe spacings is less significant compared with those in Figure 4.11. This is confirmed by calculating the slopes of the WVD coefficients. The slopes of the hologram signals at row 250 and 450 are 1.42 and 1.40, respectively.

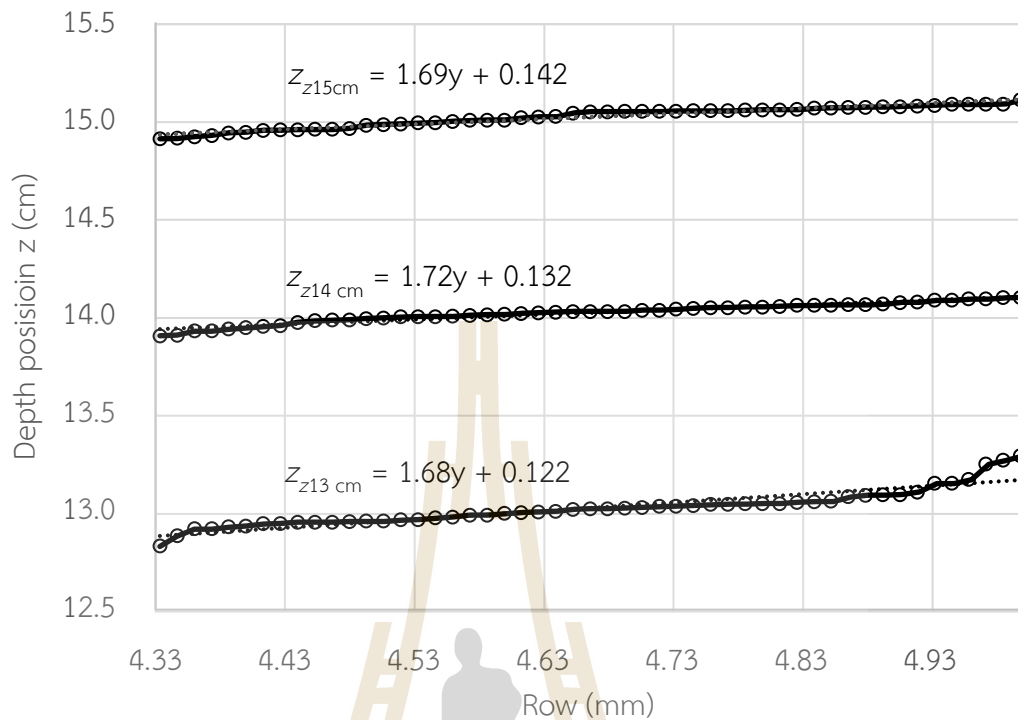


Figure 4.16 Plots of the measured depth position z for different recording distances of the holograms as a function of the row numbers represented in mm unit.

The position and size of the particle are extracted for each row of the holograms. Figure 4.16 shows the measured depth position z of the microtube for different recording distances as a function of the sensor rows. For the recording distances of 14 and 15 cm, the increases in the measured depth positions are almost linear compared to those at the distance of 13 cm. The reason for this difference is that when the microtube is oriented with the angle $\alpha < 90^\circ$, the range of the depth variation is smaller than that for the microtube parallel to the yz plane, which has the angle $\alpha = 90^\circ$.

Table 4.7 presents the errors in the depth and size measurements of the microtube oriented diagonally in the 3D space. Similar effects of the recording distance on the errors can be observed. However, the position and size measurements have higher errors than those of the microtube oriented in the yz and xz planes. These results can be understood by considering that besides the under-sampling effect caused by the recording distance, the rotated hologram fringes are sampled with a lower resolution.

Table 4.7 MAEs in the position and size measurements of the 100 μm microtube oriented diagonally in the 3D space, $\alpha = 45^\circ$, $\beta = 60^\circ$ and $\gamma = 60^\circ$ using the proposed single WVD coefficient.

Recording distance z (cm)	Mean of distance z (cm)	MAE of distance z (%)	Mean of radius a (μm)	MAE of radius a (%)
13.0	13.02	5.396	50.40	4.734
14.0	14.02	4.651	50.04	4.276
15.0	15.02	4.566	50.56	3.747

4.2.3 Reconstructions of 3D profile of the rotated particle

In this section, the reconstructions of the 3D microtube's profile using the proposed method are presented. Tables 4.8 and 4.9 present the calculated orientation angles and the length of the microtube using the proposed method for the microtubes oriented parallel to the yz plane and in the 3D space of the bounding box in Figure 3.9, respectively. In the case of the parallel orientation of the microtube with respect to the yz plane, the size δ_x in the hologram shown in Figure 4.9 is zero. When the calculated number of rows δ_y was equal to 51, the corresponding depth range δ_z can be obtained from the linear regression line of the difference depths at rows 275 and 225 shown in Figure 4.11. As a result, the orientation angle γ could be calculated using an $\arctan(\delta_y/\delta_z)$, while the microtube length p was calculated by using Eq. (3.34) with $\delta_x = 0$.

Table 4.8 The orientation angles and length of the 100 μm microtube oriented parallel to the yz plane for difference recording distances.

z (cm)	δ_x (cm)	δ_y (cm)	δ_z (cm)	α (degree)	β (degree)	γ (degree)	p (cm)
13.0	0	0.66	0.36	90	61	29	0.83
14.0	0	0.66	0.37	90	60	30	0.84
15.0	0	0.66	0.38	90	60	30	0.84

The 3D plot of the 100 μm microtubes oriented parallel to the yz plane is shown in Figure 4.17. The hologram was recorded at the recording distance z of 14 cm. In the figure, the microtube profile is plotted according to row numbers 275 – 325 of the sensors. It is apparent that the surface of the reconstructed profile is not uniform because the measured diameter in each row was slightly different.

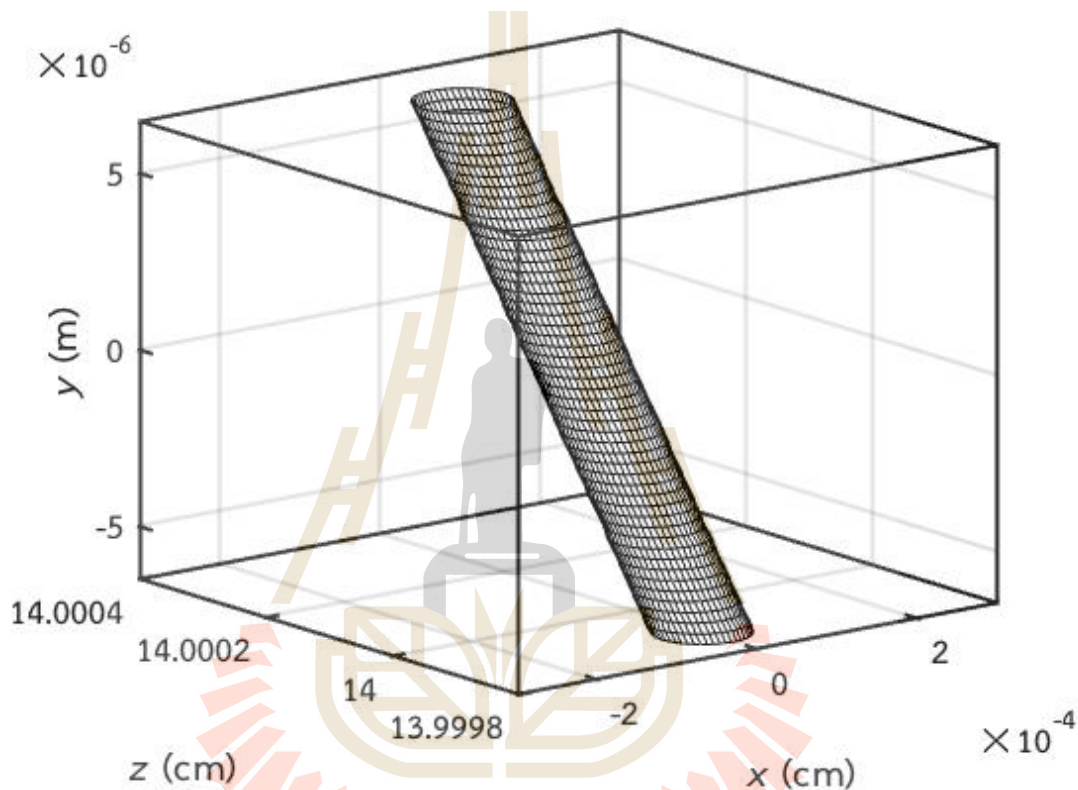


Figure 4.17 3D reconstructed profile of the 100 μm microtube profile oriented parallel in the yz plane using the proposed method. The hologram was recorded at the recording distance z of 14 cm.

In the case of the diagonal orientation, the position of the fringe center was first determined. After determining the orientation angles using Eqs. (3.31) – (3.33) discussed in Sect. 3.6, the dimensions, δx , δy , and δz , of the bounding box in Figure 3.9 were then calculated. The calculated results are presented in Table 4.9. The microtube length p is slightly longer than that in Table 4.8 because δx is not equal to zero.

Table 4.9 The orientation angles and length of the 100 μm microtube oriented diagonally in the 3D space for difference recording distances.

z (cm)	δ_x (cm)	δ_y (cm)	δ_z (cm)	α (degree)	β (degree)	γ (degree)	ρ (cm)
13.0	0.39	0.66	0.38	45	61	59	0.86
14.0	0.38	0.66	0.37	45	60	60	0.85
15.0	0.39	0.66	0.38	45	61	59	0.85

Figure 4.18 shows the 3D plot of the 100 μm microtubes oriented in the 3D space of the bounding box in Figure 3.9. The hologram was also recorded at the recording distance z of 14 cm. Since the errors in the size measurement are larger than those of the microtube oriented in the yz plane, the nonuniformity of the reconstructed surface profile is more obvious. The experimental results verify that the proposed method can be used to reconstruct the 3D profile of the line-shaped particle with arbitrary orientation from in-line holograms.

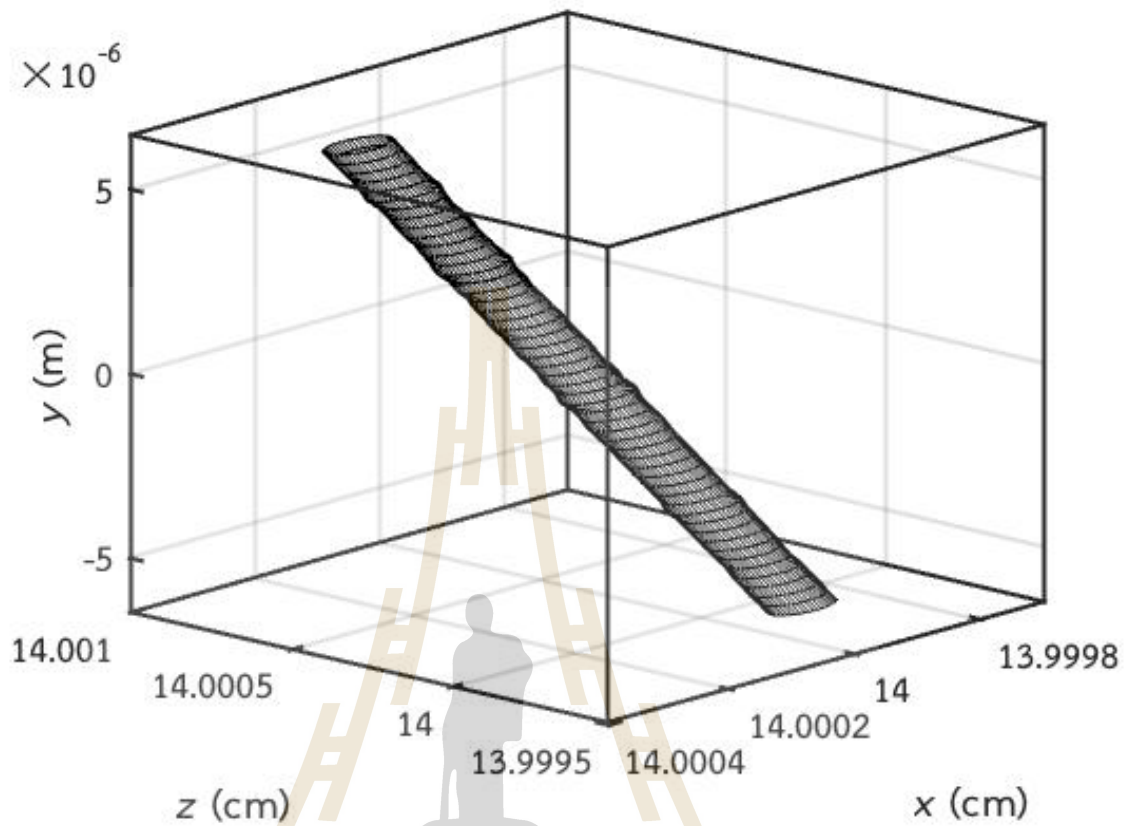


Figure 4.18 3D profile of the reconstructed particle of $z = 14$ cm from the recorded in-line hologram of a line-shaped particle with $a = 50 \mu\text{m}$ and the rotation angle $\alpha = 45$, $\beta = 60$, and $\gamma = 60$ degrees.

CHAPTER V

CONCLUSIONS AND THE FUTURE WORK

5.1 Conclusions

This thesis has proposed and experimentally demonstrated a new method for extracting the size of the line-shaped particles from the in-line holograms by using the spatial frequency information of the single pixel of the WVD coefficients with a minimum amplitude. In conjunction with the information on particle depth position obtained using the WVD, the thesis has also demonstrated the reconstruction of the 3D profiles of the line-shaped particles.

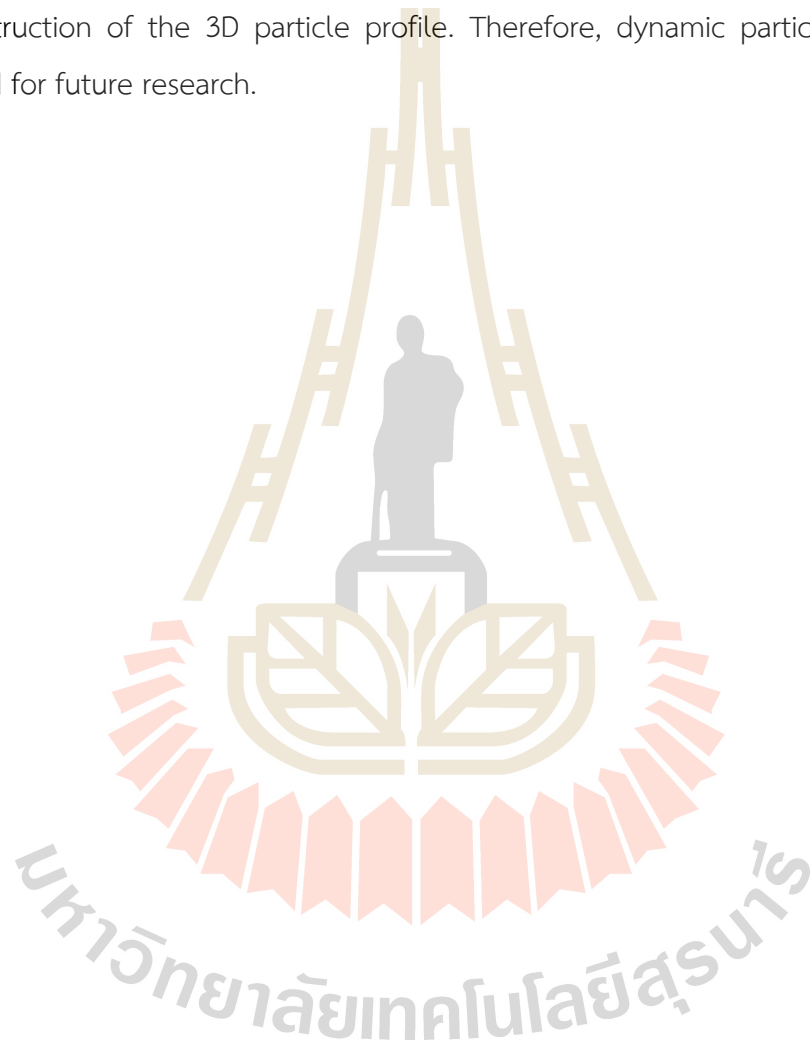
The significance of this thesis is that the particle size can be extracted without using information about the particle position. Therefore, the advantage of this proposed method is that, firstly, the error in the size measurement does not depend on the position information. Secondly, the sizing process is faster because it does not require iterative computations of the depth position of the particle.

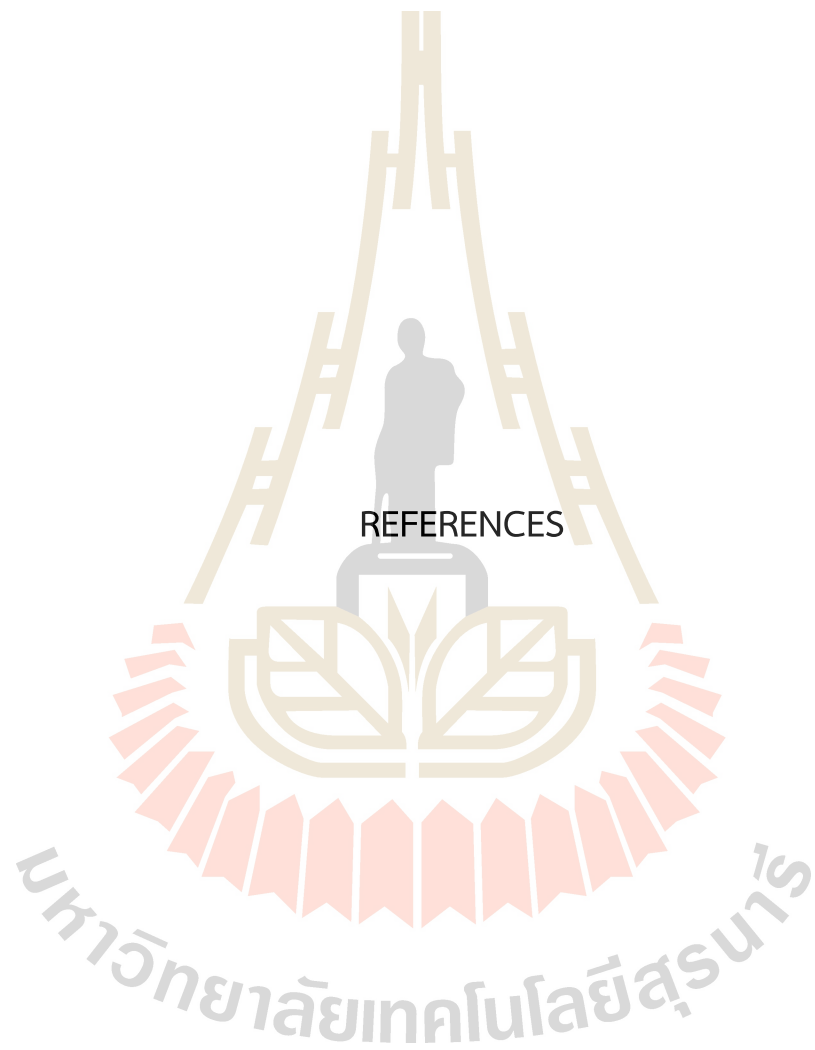
Theoretical analysis of the performance of the proposed method shows that the range of size measurement and reconstruction are dependent on the recording distance and the sensor resolution.

The feasibility of the proposed method was validated using microtubes with 80 and 100 μm diameters. The in-line holograms of the microtubes were recorded using the CCD sensors at different axial positions and orientations. The proposed WVD analysis was done using Matlab software version 2019a, run on MacOs. The experimental results show that the sizing of microtubes with different orientations can be accurately performed by using a single computation of the proposed method. The error in size measurement is higher than 1% because the low-resolution of the sensor results in the under sampling effect. The error increases as the recording distances become shorter.

5.2 Future work

A single computation method for tracking small particles together with the ability to reconstruct their shapes is highly demanded in diverse microscopic fields. As discussed in this proposed method, the WVD coefficient with the minimum amplitude can provide not only information on particle position and size but also the reconstruction of the 3D particle profile. Therefore, dynamic particle flow will be studied for future research.





REFERENCES

REFERENCES

- Abeysekera, S. S. and Boashash, B. (1991). Methods of signal classification using the images produced by the Wigner-Ville distribution. *Pattern Recognition Letters*. 12(11), 717-729.
- Bachalo, W. D. (1980). Method for measuring the size and velocity of spheres by dual-beam light-scatter interferometry. *Applied Optics*. 19, 363-370.
- Bianchi, S., Saglimbeni, F. and Leonardo, R. D. (2017). Holographic Imaging Reveals the Mechanism of Wall Entrapment in Swimming Bacteria. *Physical Review X*. 7(1), 011010.
- Boashash, B. (1988). Note on the use of the Wigner distribution for time-frequency signal analysis. *IEEE Transactions on Acoustics, Speech, and Signal Processing*. 36(9), 1518-1521.
- Bou, E., Ly, A., Roul, J., Llopis, O., Vieu, C. and Cerf, A. (2019). Compact system for in situ laser Doppler velocimetry of blood flow. *Biomedical Optics Express*. 10, 5862-5876.
- Buters, J. N. and Lendertz, J. A. (1971). Holographic and video techniques applied to engineering measurement. *Measurement and Control*. 4, 349-354.
- Buzalewicz, I., Kujawińska, M., Krauze, W. and Podbielska, H. (2016). Novel Perspectives on the Characterization of Species-Dependent Optical Signatures of Bacterial Colonies by Digital Holography. *Plos One*. 11(3), e0150449.
- Caulfield, H. J. (2004). *The Art and Science of Holography: A Tribute to Emmett Leith and Yuri Denisyuk*. SPIE Press Monograph. PM124.
- Caprio, G. D., Ferrara, M. A., Miccio, L., Merola, F., Memmolo, P., Ferraro, P. and Coppola, G. (2014). Holographic imaging of unlabelled sperm cells for semen analysis: a review. *Journal of Biophotonics*. 8(10), 779-789.

- Chuamchaitrakool, P. (2017). *Object size extraction from In-Line holograms by using Wigner-Ville distribution*. Doctoral dissertation, Laser Technology, Science, Suranaree University of Technology, Thailand, 20.
- Chuamchaitrakool, P., Widjaja, J. and Yoshimura, H. (2015). Holographic particle sizing using Wigner–Ville distribution. *Optics and Lasers in Engineering*. 67, 186-190.
- Dawprateep, S. (2015). *Extraction of 3-D object position from in-line holograms by using minimum coefficient of Wigner-Ville distribution*. Master dissertation, School of Physics, Science, Suranaree University of Technology, Thailand, 23-24.
- Dawprateep, S. and Widjaja, J. (2021). Single-pixel holographic rod-shaped particle sizing without depth search using Wigner-Ville distribution. *Optics and Lasers in Engineering*. 142, 106606, ISSN 0143-8166.
- Funamizu, H. and Aizu, Y. (2018). Three-dimensional quantitative phase imaging of blood coagulation structures by optical projection tomography in flow cytometry using digital holographic microscopy. *Journal of Biomedical Optics*. 24(3), 031012.
- Gabor, D. (1948). A new microscopic principle, *Nature*. 161, 777-778.
- Goodman, J. W. (1996). *Introduction to Fourier Optics*. 2nd ed., Singapore: McGraw-Hill.
- Goodman J. W. and Lawrence R. W. (1967). Digital image formation from electronically detected holograms. *Applied Physics Letters*. 11, 77-79.
- Hariharan, P. (2007). *Basics of Interferometry (Second Edition)*. Academic Press, 111-120.
- Khanam, T., Rahman, M. N., Rajendran, A., Kariwala, V. and Asundi, A. K. (2011). Accurate size measurement of needle-shaped particles using digital holography. *Chemical Engineering Science*. 66(12), 2699-2706.
- Kilpatrick, D., Tyberg, J. V. and Parmley, W. W. (1982). Blood Velocity Measurement by Fiber Optic Laser Doppler Anemometry. *IEEE Transactions on Biomedical Engineering*. BME 29(2), 142-145.
- Kim, M. K. (2010). Principles and techniques of digital holographic microscopy, *SPIE Reviews*. 1(1), 018005.
- Kim, S. and Lee, S. J. (2007). Measurement of 3D laminar flow inside a micro tube using micro digital holographic particle tracking velocimetry. *Journal of Micromechanics and Microengineering*. 17(10), 2157-2162.

- Kohli, R. (2012). *Developments in Imaging and Analysis Techniques for Micro and Nanosize Particles and Surface Features*. Chapter 5, Developments in Surface Contamination and Cleaning, William Andrew Publishing, 215-306.
- Langehanenberg, P., Kemper, B., Dirksen, D. and Bally G. V., (2008). Autofocusing in digital holographic phase contrast microscopy on pure phase objects for live cell imaging. *Applied Optics*. 47, D176-D182.
- Latychevskaia, T., Formanek, P., Koch, C. T. and Lubk, A. (2010). Off-axis and inline electron holography: Experimental comparison, *Ultramicroscopy*. 110(5), 472-482.
- Li, H., Chen, X., Chi, Z., Mann C., and Razi, A., (2020). Deep DIH: Single-Shot Digital In-Line Holography Reconstruction by Deep Learning. *IEEE Access*. 8, 202648-202659.
- McCartney, M. R., Lins, U., Farina, M., Buseck, P. R. and Frankel, R. B. (2001). Magnetic Microstructure of Bacterial Magnetite by Electron Holography. *European Journal of Mineralogy*. 13(4), 685-689.
- Memmo, P., Miccio, L., Merola, F., Gennari, O., Netti, P. A. and Ferraro, P. (2014). 3D morphometry of red blood cells by digital holography. *Cytometry*. 85(12), 1030-1036.
- Memmo, P., Miccio, L., Paturzo, M., Caprio, G. D., Coppola, G., Netti, P. A. and Ferraro, P. (2015). Recent advances in holographic 3D particle tracking. *Advances in Optics and Photonics*. 7, 713-755.
- Merrill, D., An, R., Turek, J. and Nolte, D. D. (2015). Digital holography of intracellular dynamics to probe tissue physiology. *Applied Optics*. 54(1), A89-A97.
- Meyer-Arendt, J. R. (1989). *Introduction to Classical and Modern Optics, Third Edition*. Prentice-Hall, Englewood Cliffs, New Jersey, 346-355.
- Misono, T. (2019). *Dynamic Light Scattering (DLS)*. In: Abe M. (eds) *Measurement Techniques and Practices of Colloid and Interface Phenomena*. Springer, Singapore.
- Molaei, M. and Sheng, J. (2014). Imaging bacterial 3D motion using digital in-line holographic microscopy and correlation-based de-noising algorithm. *Optics Express*. 22, 32119-32137.

- Morrison, K. E. (1995). Cosine products. Fourier transforms and random sums. *The American Mathematical Monthly*. 102(8), 716-724.
- Murata, K., Fujiwara, H. and Asakura, T. (1970). Several problems in in-line Fraunhofer holography for bubble-chamber track recording. in Proc. Conf. on Engineering Use of Holography. *Cambridge University Press*. Cambridge. United Kingdom: N. p., 289-300.
- Nair, B. S. (2002). *Digital electronics and logic design*. India. PHI Learning Pvt. Ltd.
- Pachori, R. B. and Nishad, A. (2016). Cross-terms reduction in the Wigner-Ville distribution using tunable-Q wavelet transform, *Signal Processing*. 120, 288-304.
- Perucho, B. and Micó, V. (2014). Wavefront holoscopy: application of digital in-line holography for the inspection of engraved marks in progressive addition lenses. *Journal of Biomedical Optics*. 19(1), 16017.
- Qiu, P. (2017). The feasibility of automatic focusing in digital holography by using Fresnel transform as numerical holographic reconstruction algorithm. *Optik*. 137, 220-227.
- Schnars, U. and Jüptner, W. (1994). Direct recording of holograms by a CCD target and numerical reconstruction. *Applied Optics*. 33(2), 179-181.
- Seo, K. W. and Lee, S. J. (2014). High-accuracy measurement of depth-displacement using a focus function and its cross-correlation in holographic PTV. *Optics Express*. 22, 15542-15553.
- Shao, S., Li, C. and Hong, J. (2019). A hybrid image processing method for measuring 3D bubble distribution using digital inline holography, *Chemical Engineering Science*. 207, 929-941.
- Soontaranon, S., Widjaja, J. and Asakura, T. (2008). Extraction of object position from in-line holograms by using single wavelet coefficient. *Optics Communications*. 281(6), 1461-1467.
- Tyler, G. A. and Thompson, B. J. (1976). Fraunhofer holography applied to particle size analysis: a reassessment. *Optica Acta*. 23, 685-700.
- Ville, J. (1948). Théorie et applications de la notion de signal analytique. *Cables et Transmissions*, 2A(1), 61-74.

- Wereley, S. T. and Meinhart, C. D. (2010). Recent Advances in MicroParticle Image Velocimetry. *Annual Review of Fluid Mechanics*. 42, 557-576.
- Widjaja, J., Dawprateep, S. and Chuamchaitrakool, P. (2017). Experimental extractions of particle position from inline holograms using single coefficient of Wigner-Ville analysis. *Optical Engineering*. 56(7), 074103.
- Wigner, E. (1932). On the Quantum Correction for Thermodynamic Equilibrium. *American Physical Society*. 40(5), 749-759.
- Willert, C. E. and Gharib, M. (1991). Digital particle image velocimetry. *Experiments in Fluids*. 10, 181-193.
- Wopschall, R. H. and Pampalone, T. R. (1972). Dry Photopolymer Film for Recording Holograms. *Applied Optics*. 11, 2096-2097.
- Xia, D. F., Xu, A. L. and Qi, F. (1999). A Proof of the Arithmetic Mean-Geometric Mean-Harmonic Mean Inequalities. *RGMIA Research Report Collection* 2(1), 85-87.
- Xie, L., Dou, X. Q. and Zhou, J. (2016). Sizing charged particles by phase Doppler anemometry. *Applied Optics*. 55(12), 3279-3286.
- Yeh, Y. and Cummins, H. Z. (1964). Localized Fluid Flow Measurements with an He-Ne Laser Spectrometer. *Applied Physics Letters*. 4 (10), 176.
- Yu, L. and Kim, M. K. (2005). Wavelength-scanning digital interference holography for tomographic three-dimensional imaging by use of the angular spectrum method. *Optics Letters*. 30, 2092-2094.
- Zhang, Y., Bo, Y., Wu, Y., Wu, X., Huang, Z., Zhou, J. and Cen, K. (2014). Flow behavior of high-temperature flue gas in the heat transfer chamber of a pilot-scale coal-water slurry combustion furnace. *Particuology*. 17, 114-124.

CURRICULUM VITAE

Name : Saowaros Dawprateep

Date of Birth : May 11, 1990

Place of Birth : Chaiyaphum, Thailand

Education : B.Sc. Department of Physics, Khon Kaen University, Thailand 2013

Ms.Sc. School of Physics, Suranaree University of technology
Thailand, 2015

Publications :

- Dawprateep, S. and Widjaja, J. (2021). Single-pixel holographic rod-shaped particle sizing without depth search using Wigner-Ville distribution. *Optics and Lasers in Engineering*. 142, 106606, ISSN 0143-8166.

Awards : -

Grants and Fellowships : -

Position and Place of Work : -

Scholarship :

- SUT Graduate Scholarships

มหาวิทยาลัยเทคโนโลยีสุรนารี